Honokiol Nanoscale Drug Delivery System Ameliorates the Cognitive Deficits in Tgcrnd8 Mice of Alzheimer's Disease via Inhibiting Neuropathology and Modulating Gut Microbiota

Chang Qu
Chinese University of Hong Kong https://orcid.org/0000-0002-5494-3245
Qiao-Ping Li
Guangzhou University of Chinese Medicine
Zi-Ren Su
Guangzhou University of Chinese Medicine
Siu-Po Ip
Chinese University of Hong Kong
Qiu-Ju Yuan
Chinese University of Hong Kong
You-Liang Xie
Guangzhou University of Chinese Medicine
Qing-Qing Xu
Chinese University of Hong Kong
Wen Yang
Chinese University of Hong Kong
Yan-Feng Huang
Chinese University of Hong Kong
Yan-Fang Xian
Chinese University of Hong Kong
Zhi-Xiu Lin (linzx@cuhk.edu.hk)
Chinese University of Hong Kong

Research article

Keywords: Honokiol nanoscaledrug delivery system, TgCRND8 mice, Cognitive deficits, Neuroinflammation, Tau protein hyperphosphorylation, Gut microbiota

DOI: https://doi.org/10.21203/rs.3.rs-41611/v1

Abstract

Background

Honokiol (HO) exerts neuroprotective effects in several animal models of Alzheimer's disease (AD), but the poor dissolution hampers its bioavailability and therapeutic efficacy. A novel honokiol nanoscale drug delivery system (Nano-HO) with smaller size and excellent stability was developed in this study to improve the solubility and bioavailability of HO.

Methods

Male TgCRND8 mice were administered with Nano-HO or HO at the same dosage (20 mg/kg) by oral gavage daily for 17 consecutive weeks, followed by assessment of the spatial learning and memory functions with the Morris Water Maze test (MWMT).

Results

Nano-HO and HO could significantly improve cognitive deficits and inhibit neuroinflammation via suppressing the levels of tumor necrosis factor (TNF-α), interleukin 6 (IL-6) and IL-1β in the brain, preventing the activation of microglia (IBA-1) and astrocyte (GFAP), and reducing β-amyloid (Aβ) deposition in the cortex and hippocampus of TgCRND8 mice. In addition, Nano-HO and HO could modulate amyloid precursor protein (APP) processing and phosphorylation via suppressing β-secretase including β-site APP cleaving enzyme-1 (BACE-1) and phosphorylated APP (Thr 668), inhibiting γ-secretase including presenilin-1 (PS-1) and anterior pharynx-defective-1 (APH-1), as well as enhancing Aβ-degrading enzymes such as insulin degrading enzyme (IDE) and neprilysin (NEP). Moreover, Nano-HO remarkably inhibited tau hyperphosphorylation via decreasing the levels of p-tau (Thr 205) and p-tau (Ser 404), as well as regulating tau-related apoptosis proteins including caspase-3 and Bcl-2. Furthermore, Nano-HO and HO markedly attenuated the ratios of p-JNK/JNK and p-35/CDK5, while enhancing the ratio of p-GSK-3β (Ser9)/GSK-3β. On the other hand, Nano-HO and HO prevented the alterations on the composition of gut microbiota in TgCRND8 mice.

Conclusions

Nano-HO was more effective than regular HO in improving cognitive impairments in TgCRND8 mice via inhibiting Aβ deposition, tau hyperphosphorylation and neuroinflammation through suppressing the activation of JNK/CDK5/GSK-3β signaling pathway. Nano-HO was also more potently modulate the gut microbiota community to protect its stability as compared with that of regular HO. Our results amply indicated that HO with nano-sized drug delivery system has good potential for further development into therapeutic agent for AD treatment.

Background

Alzheimer's disease (AD) is a neurodegenerative disease clinically characterized by progressive and irreversible cognitive impairments including learning and memory deficits. Although the etiology of AD remains vague, aggressive amyloid-β (Aβ) deposition, intraneuronal neurofibrillary tangles (NFTs) and chronic neuroinflammation are the classic hallmarks of AD pathology [1]. Aβ is a proteolytic product of transmembrane amyloid precursor protein (APP) by amyloidogenic cleavage, which is sequentially processed by β-secretases (e.g., p-APP (Thr 688), β-site APP cleaving enzyme-1 (BACE-1)), γ-secretases (e.g., anterior pharynx-defective-1 (APH-1) and presenilin-1 (PS-1)) and Aβ-degrading enzymes (e.g., insulin degrading enzyme (IDE) and neprilysin (NEP) [2]. Accumulation of Aβ surrounded by dystrophic neurites attributes to the formation of senile plaques, then responsible for the cognitive dysfunction of AD [3–5]. On the other hand, tau hyperphosphorylation in the NFTs is triggered by the imbalance of the kinase/phosphatase system, including c-Jun N-terminal kinase (JNK), glycogen synthase kinase 3β (GSK-3β) and cyclin-dependent kinase 5 (CDK5) [6]. These enzymes regulate the signaling pathway of Aβ and tau hyperphosphorylation. Among them, GSK-3β participates in the process of Aβ production and Aβ-mediated neuronal death by increasing tau hyperphosphorylation. Additionally, it has been reported that tau protein phosphorylation was affected by the interaction of Aβ and CDK5, which leads to cleavage of adjacent proteins p-35 [6]. Abnormal APP processing leads to the secretion of Aβ, which is known to affect GSK-3 kinases, leading to tau phosphorylation and aggregation of tau filaments, finally forming huge insoluble masses of NFTs in neurons [7]. The aggregation of Aβ plaques and tau tangles is followed by microglia recruitment surrounding plaques, microglial activation and local inflammatory response, thus the occurrence of neurotoxicity. In addition, activation of caspase-3 stabilizes BACE, leading to an increase in the Aβ production in AD brains [8]. Currently, available drugs for AD can only ameliorate symptoms, but are unable to reverse or even slow down the disease process [9–11]. Given that the multiple factors involved in AD pathogenesis, multi-target drug development is now perceived as a more promising therapeutic strategy for AD treatment.

Chinese herbal medicines are known to possess multiple components and exert therapeutic effects through multiple targets for prevention and treatment of diseases. Therefore, they may be promising sources for discovering agents for AD treatment [12]. Honokiol (HO, $C_{18}H_{18}O_2$, the chemical structure is shown in Fig. 1A), is a major active compound isolated from the dried bark of *Magnoliae Officinalis* Rehd. et wils. Recent studies have indicated that HO possesses neuroprotective effect against the cerebral ischemia/reperfusion-induced memory dysfunction, the stroke-induced brain damage and the age-related memory and learning deficits in SAMP8 mice [13–15]. In addition, our previous study indicated that HO could reduce the learning and memory impairments in the scopolamine-treated mice via inhibiting acetylcholinesterase (AChE) activity and ameliorating neuroinflammation [16]. HO could also prevent the Aβ-induced neurotoxicity via suppression of GSK-3β and β-catenin signaling pathway in PC12 cells [17]. Nevertheless, the poor dissolution severely hampers its bioavailability. To overcome the intrinsic chemical solubility barrier of HO, we applied nano-particle drug delivery system (Nano-DDS) to formulate HO (thereafter termed "Nano-HO"), which is a universal approach allowing slow release in the body. Nano-

DDS is composed of surfactant(s), cosurfactant, oil and drugs, which spontaneously form oil-in-water (O/W) microemulsion with nanometric droplet size (20–100 nm) under mild agitation [18]. Tiny globule size of Nano-DDS provides a large interfacial surface area, thus improving drug absorption and bioavailability by enhancing drug release and membrane permeation, as well as reducing pre-systemic metabolism [19].

Gut microbiota, the large number of commensal microorganisms in the intestine, is markedly different in the gut composition between AD patients and healthy people [20, 21]. Gut microbiota has been reported to be involved in the development of AD by producing neurotransmitter-like products, forming amyloid and inducing low levels of inflammatory response [22–25]. Neurotransmitters and neurotoxic substances produced by certain types of bacteria can enter the brain through the systemic circulation to further affect nerve function, and the phenomenon is generally referred to as the “microbiota-gut-brain axis” [26]. Previous study has demonstrated a strong association between cognitive dysfunction in SAMP8 mice and abnormal gut microbiota composition [27]. TgCRND8 mice, a well-characterized APP transgenic mouse model of AD, shows a close association among Aβ deposition, neuroinflammation and tau hyperphosphorylation and cognitive impairments [28–30]. Based on these findings, TgCRND8 mice are believed to be suitable for discovering anti-AD agents in preclinical study.

In this study, we aimed to apply Nano-DDS to enhance the solubility and bioavailability of HO, and the Nano-HO was evaluated by physicochemical properties of droplet size, poly-dispersity index (PDI), zeta potential (ZP) and morphology. Meanwhile, *in vitro* release and pharmacokinetics studies were conducted to compare the bioactivity of HO and Nano-HO. Moreover, we explored the cognitive deficit-ameliorating effects of Nano-HO and HO and illustrated the underlying molecular mechanisms on Aβ deposition, tau hyperphosphorylation, Aβ plaque-associated neuroinflammation, JNK/CDK5/GSK-3β signaling pathway as well as gut microbiota in TgCRND8 transgenic mice.

Methods

Chemical and reagents

Honokiol (purity ≥ 98% by high performance liquid chromatography (HPLC) analysis) was provided by Prof. Zi-Ren Su of the Guangzhou University of Chinese Medicine. Its identity was confirmed by comparing its ^{1}H NMR and ^{13}C NMR spectra with that published in the literature [31]. Donepezil hydrochloride (purity ≥ 98%) was purchased from Sigma-Aldrich (Cat No.: D6821, St. Louis, MO, USA). Kolliphor® HS-15 (PEG-15-hydroxystearate; BASF, Ludwigshafen, Germany), PEG-400 was obtained from Sigma-Aldrich (St Louis, MO, USA). Medium-chain triglycerides (C8, MCT) was purchased from Guangdong Mingkang Flavors & Fragrances Co., Ltd. (Guangzhou, Guangdong, China). All other chemicals and reagents used in this study were of analytical grade.

Preparation of Nano-HO

Nano-HO was prepared using HS-15, PEG-400, and MCT at the ratio of 4:2:1 (w/w/w). HO was dissolved in MCT (oil) and then mixed with HS-15 (surfactant) and PEG-400 (co-surfactant) in a gentle magnetic stirring at 300 rpm for 30 min at 25 °C. After pre-equilibrium at room temperature, the solution was diluted 100-fold with double-distilled water and stirred till clear and slightly bluish.

Characterization of Nano-HO

The droplet size, ZP and PDI were measured at 25 °C by a Zetasizer Nano ZS (Malvern Instruments, Britain) based on dynamic light scattering. The morphology of Nano-HO was determined by Hitachi-HT7700 transmission electron microscope (Hitachi-Technologies Corp., Tokyo, Japan). Samples with a 500-fold dilution were placed on a copper grid (400 mesh). After the samples were dried, they were stained with phosphotungstic acid (2%) for 30 s at room temperature to form a thin film and then observe under transmission electron microscope (TEM).

Animals

Male Sprague Dawley (SD, weighing 230–250 g) rats were obtained from the Laboratory Animal Services Centre, The Chinese University of Hong Kong. Male TgCRND8 mice were crossed with female non-transgenic mice on the hybrid C3H/He-C57BL/6 background to breed a colony of experimental animals. Non-transgenic littermates that did not express human APP transgene were identified as wild-type mice and used as negative controls for experiments. Both rats and mice were maintained on a 12 h light/dark cycle under controlled humidity (50 ± 10%) and temperature (24 ± 2 °C), with access to food and water *ad libitum*. The experimental procedures were approved by the Animal Experimentation Ethics Committee of The Chinese University of Hong Kong (Ref. No. 18/108/GRF).

In vitro **release of Nano-HO and HO**

The *in vitro* release of Nano-HO and HO was determined by a modified method described previously [32]. briefly, 5 mL of Nano-HO (containing 5 mg HO) and HO (5 mg HO suspended in 0.5% CMC-Na as control) were placed into a dialysis bag (molecular weight cut-off of 8000–14000 Da) surrounded by 100 mL of phosphate-buffered saline (PBS, pH 7.4) and incubated at 37 °C in an incubator shaker (100 rpm/min). Two hundred microliter of dialysates was collected at 0, 30, 60, 120, 240, 360, 480, 720 and 1440 min while same volume of fresh PBS (37 °C) was subsequently added into the dialysis solution. After centrifugation at 10000 rpm for 10 min, the dialysates were collected and passed through a 0.22 μm filter. For HPLC analysis, the samples were sonicated in 0.2 mL of methanol and detected three times by normalizing the results against the standard curve of HO. The HO released from Nano-DDS and free HO by percentages were plotted against time.

Pharmacokinetics study

Male SD rats (weighing 230–250 g) were randomly assigned into Nano-HO group and HO group (n = 5) containing the same content of HO (80 mg/kg). The dosage of HO was selected based on a previous report [32]. Under anesthetization with diethyl ether, the rat blood samples (0.30 mL each) were collected at 5, 15, 30, 45, 60, 90, 120, 240, 360, 480, 720, and 1440 min from the rat eye socket veins via

heparinized capillary tubes after drugs treatment. After centrifugation at 3500 rpm for 10 min at 4 °C, plasma samples were collected and stored at -20 °C for further analysis. The method of plasma sample preparation was determined as previously described [32]. Briefly, 200 μL plasma was mixed with 50 μL docetaxel (800 μg/mL, internal standard) and 350 μL methanol in a vortex mixer for 30 s. The mixture was centrifuged at 12000 rpm for 15 min at 4 °C. Then, all supernatants were transferred to the auto-sampler vials for introduction into the HPLC system. The analysis was performed with a Shimadzu SIL-20 AHPLC system. Separation was achieved on a unisol C_{18} column (5 μm, 100 A°, 4.6 × 250 mm, Agela Technologies, Tianjin, China) and eluted on an isocratic mobile phase composed of methanol and distilled water (76:24, v/v) at a constant flow rate of 1.0 mL/min.

Analysis software DAS (Version 3.0; Data Analysis System, Shanghai, China) was used to assess the pharmacokinetic parameters according to the non-compartmental model. With the concentration time curve ranging from 0 to 12 hours (AUC_{0-12}), the maximum plasma concentration (C_{max}), and peak time (T_{max}) were obtained directly from the plasma concentration vs time curve. The mean residence time (MRT_{0-12}), and the biological half-life time ($t_{1/2}$) were estimated from the terminal linear portion of the plasma concentration-time profile. The comparative t-test was applied using SPSS software to assess the statistical significance.

Polymerase chain reaction (PCR) for genotyping

All mice were subjected to genotyping for the APP transgene before experiments as described in our previous study [33]. PCR analysis was performed on genomic DNA isolated from ear using the following primers: Forward- TGTCCAAGATGCAGCAGAACGGCTAC, Reverse - AAACGCCAAGCGCCGTGACT. Those mice with APP transgene were identified as transgenic mice, while those without APP transgene as wild type (WT) ones.

Experimental design and drugs treatment in TgCRND8 mice

Three-month-old male mice were divided into 5 groups with 9 mice in each group: (1) WT group; (2) TgCRND8 (Tg) + vehicle group; (3) Tg + HO (20 mg/kg) group; (4) Tg + Nano-HO (20 mg/kg) group; (5) Tg + Donepezil (5 mg/kg) group. The dosage of HO was selected based on the previous studies [16, 34, 35]. Donepezil was chosen as a positive control and dissolved in normal saline. HO was suspended in 0.5% sodium carboxymethylcellulose (CMC-Na). Mice were administered with HO, Nano-HO and donepezil by gavage once daily for 17 consecutive weeks, whereas mice in the WT group and Tg + vehicle group received the same volume of vehicle (0.5% CMC-Na) for the same duration. After drug treatment, the spatial learning and memory functions were assessed by Morris Water Maze test (MWMT). Figure 3A showed the experimental design and schedule.

Morris Water Maze test (MWMT)

MWMT was performed to assess spatial learning and memory functions [36]. The modular MWMT with a video tracking software of SuperMaze V2.0 was purchased from Xinruan Information Technology Co. Ltd (Shanghai, China). A tank was acted as a maze, and the diameter and the height of the maze were 180

and 70 cm respectively. The maze was filled with water at 25 °C and divided into four equal quadrants. A circular escape platform with 10 cm of diameter was fixed in the midpoint of one quadrant that 2 cm beyond the water surface. The tank was located in a test room that contained various prominent visual color pictures (e.g., Triangle, circle, quadrate, etc.). The mice were trained for consecutive 4 days to find the platform. There were 3 trials for each mouse per day, and the inter-trial interval of each trial was 60 s. To minimize the performance differences caused by circadian rhythmicity, the MWMT was performed between 9:00 and 18:00. In each trial, we placed the mice gently in one quadrant randomly with its nose pointing toward the wall and allowed them to find the escape platform. Each mouse was given 60 s to find the platform and allowed to stay on it for 30 s. If a mouse did not find the platform within 60 s, the mouse was placed on the circular platform for 30 s before the next trial, and the escape latency (finding the submerged platform) was recorded as 60 s. To determine the ability of spatial learning, the time of the mouse spent to reach the platform was recorded. On day 5, a probe test of spatial memory was conducted by removing the platform, then the time spent in the target quadrant and the number of crossing the platform quadrant were recorded.

Brain sample processing

Twenty-four hours after MWMT, 6 mice in each group were euthanized with ketamine and xylene, then the brain tissues were removed rapidly and separated into two hemispheres equally for western blotting analysis and ELISA assay. All samples were stored at − 80 °C before further analysis.

For immunofluorescence analysis, 3 mice in each group were deeply anesthetized using xylene and ketamine and transcardially perfused with 0.9% saline followed by buffered 4% paraformaldehyde. Afterwards, the brain tissues were post-fixed in 4% paraformaldehyde overnight at 4 °C, then stored in 30% at 4 °C sucrose until sectioned.

Cytokines determination

The brain tissues of mice were homogenized vigorously in 0.8 mL of lysis buffer (contained in kits). After incubation on ice for 20 min, the homogenates were centrifuged at 12000 rpm for 20 min at 4 °C. Protein concentrations were determined by Pierce™ BCA protein Assay kit (Catalog No.: 23227, Thermo Fisher Scientific). The levels of TNF-α (Catalog No.: ab100747), IL-6 (Catalog No.: ab100712) and IL-1β (Catalog No.: ab100704) in the supernatants were determined using commercially available ELISA kits (Abcam, Cambridge, UK) according to the manufacturer's instructions. The levels of TNF-α, IL-6 and IL-1β were expressed as pg/mg protein.

Western blotting

For preparation of protein lysates, frozen brain tissues were homogenized in RIPA lysis buffer (Catalog No.: 89900, Thermo Fisher Scientific) which contains 1% Protease/Phosphatase Inhibitor Cocktail (Catalog No.: 78442, Thermo Fisher Scientific) for 30 min on ice. After centrifugation at 14,000 rpm at 4 °C for 15 min, the supernatants were collected. Protein concentrations were determined by Pierce™ BCA protein assay kit (Catalog No.: 23227, Thermo Fisher Scientific). Equal amounts of proteins of different

samples were loaded. The proteins were separated by SDS-PAGE and then transferred to PVDF membranes. After being blocked with 5% (w/v) non-fat milk in TBST at room temperature for 2 h, the PVDF membranes were incubated at 4 °C overnight with primary antibodies against CTFs (Catalog No.: A8717, Sigma), p-APP (Thr688) (Catalog No.: 6986S, Cell Signaling Technology), BACE-1 (Catalog No.: SAB2100200, Sigma), APH-1 (Catalog No.: PRS4001, Sigma), PS-1 (Catalog No.: sc-365450, Santa Cruz), IDE (Catalog No.: sc-393887, Santa Cruz), NEP (Catalog No.: AP1126-SP, R&D Systems), p-tau (Thr 205) (Catalog No.: sc-101817, Santa Cruz), p-tau (Ser 396) (Catalog No.: ab109390, Cell Signaling Technology), p-tau (Ser 404) (Catalog No.: ab92676, Cell Signaling Technology), tau (Tau 46) (Catalog No.: sc-32274, Santa Cruz), caspase-3 (Catalog No.: sc-7148, Santa Cruz), B cell lymphoma-2 (Bcl-2) (Catalog No.: sc-7382, Santa Cruz), p-JNK (Catalog No.: sc-12882, Santa Cruz), JNK (Catalog No.: sc-7345, Santa Cruz), p-GSK-3β (Ser 9) (Catalog No.: 9336s, Cell Signaling Technology), GSK-3β (Catalog No.: sc-9166, Santa Cruz), CDK5 (Catalog No.: 2506, Cell Signaling Technology), p35/25 (Catalog No.: 2680, Cell Signaling Technology) and β-actin (Catalog No.: sc-69879, Santa Cruz). After rinsing with TBST for 5 min × 3 times, the PVDF membranes were then incubated with secondary antibodies against anti-mouse (Catalog No.: 7076s, Cell Signaling Technology), anti-rabbit (Catalog No.: 7074s, Cell Signaling Technology) and donkey anti-goat (Catalog No.: sc-2020, Santa Cruz) for 2 h at room temperature. After rinsing with TBST for 5 min × 3 times, the protein bands were visualized by the Pierce™ ECL western blotting substrate (Catalog No.: 32106, Thermo Fisher Scientific). The intensity of each band was imaged by acer c300 (Azure systems, Mumbai, India) and analyzed using Image J software (NIH Image, MD, USA).

Immunofluorescence assay

Coronal brain sections were sectioned at a thickness of 30 μm using cryostat (Leica CM1850, Leica Microsystems GmbH, Wetzlar, Germany) and stored at 4 °C in 0.1 M PB. Prior to staining, the sections were immersed in 0.25% trypsin and incubated at 37 °C for 30 min to achieve antigen retrieval. Then the sections were rinsed in PB three times for 15 min, followed by permeabilization in 0.1 M PB solution with 0.3% Triton, and subsequently incubated overnight at room temperature on a shaker with primary antibodies against anti-β-amyloid 17–24 antibody Catalog No.: A5213, Sigma, USA), anti-GFAP polyclonal antibody (Catalog No.: C106874, Sigma) and anti-IBA-1 antibody (Catalog No.: 019-19741, Wako) in the blocking solution. On the following day, the sections were rinsed with PB three times for 15 min. Next, the sections were incubated with donkey anti-mouse secondary antibody conjugated with Alexa Fluor 488, donkey anti-rabbit secondary antibody conjugated with Alexa Fluor 594 and donkey anti-mouse secondary antibody conjugated with Alexa Fluor 647 (1:500) (Life Technology/Thermo Fisher Scientific, Waltham, MA) for 2 h at room temperature in dark, followed by rinsing with PB three times for 15 min. The sections were then mounted on microscope slides (Lab'IN Co, NT, Hong Kong) and cover-slipped using fluorescence mounting medium (Dako North America, Inc., CA, USA). Immunofluorescent images were captured using a Zeiss fluorescent inverted microscope (Zeiss, Gottingen, Germany) equipped with an ORCA-Flash 4.0 v2 digital CMOS camera (Hamamatsu Photonics, Iwata City, Japan). The quantification was analyzed by two investigators who were blinded to the animal grouping using Image J software (NIH, Bethesda, MD, USA).

Molecular docking for HO on human BACE-1

SwissDock (URL: www.swissdock.ch) was used to perform the molecular docking analysis of HO on BACE-1. The 3D structure of HO was downloaded from Swissdock database. Crystal structure of BACE-1 in the complex with NLG919 analogue (PDB ID, 1SGZ) was downloaded from RCSB PDB Bank (http://www.pdb.org). The docking results were analyzed using UCSF Chimera 1.11.1 (RVBI, UCSF; San Francisco, CA, USA). Ligand binding results with negative △G values were regarded as having an affinity in the binding between HO and BACE-1. The number of possible hydrogen bonds and the bond lengths were determined by the Find H-Bond tool in UCSF Chimera. All docking procedures were performed using Windows 10.

Fecal DNA extraction and Illumina miseq sequencing

Fecal samples of the mice were collected into 2 mL tubes and stored at -80 °C after frozen in liquid nitrogen. Fecal genomic DNA was extracted with OMGA-soil DNA kit as per the manufacturer's instruction. Hypervariant region V4 of bacterial 16S rRNA gene was amplified with the forward primer 515 F (5'-GTGCCAGCMGCCGCGGTAA-3') and reverse primer 806R (5'-GGACTACHVGGGTWTCTAAT-3') by PCR. Products were purified with Agencourt Ampure XP beads (AGENCOURT, Beckman coulter, US) to remove the unspecific products. The quality of sequencing library was analyzed by Agilent 2100 bioanalyzer instrument (Agilent DNA 1000 Reagents, CA, USA) to determine the average molecular weights. Purified amplicons were sequenced pair end on the Illumina MiSeq PE300 System at Beijing Genomics Institute.

Raw fastq files were quality-filtered using QIIME61 (v1.17). Reads which could not be assembled were discarded. The taxonomy of each sequence was analyzed by RDP Classifer (v2.2) against Silva (v119) 16S rRNA database with 80% confidence threshold. Rarefaction analysis was performed by Mothur (v1.31.2) and α-diversity indexes were compared using rarefed data. Principal component analysis (PCA) plot was implemented by R programming language. Significant changes in relative abundance of microbial taxa were detected by linear discriminant analysis effect size (LEfSe).

Statistical analysis

All data were presented as the mean ± SEM. Group differences in the escape latency in the Morris water maze training task were analyzed using two-way analysis of variance (ANOVA) with repeated measures, with the factors being treatment and training day. The other data were analyzed using one-way ANOVA followed by Post-hoc Bonferroni's test to detect inter-group differences. Group differences between HO group and Nano-HO group were analyzed using unpaired t test. GraphPad Prism software (Version 8, GraphPad Software, Inc., CA, USA) was used to perform the statistical analysis. A difference was considered statistically significant when the $p < 0.05$.

Results

Droplet size, zeta potential, morphology and appearance of Nano-HO

As shown in Fig. 1B-C, the mean droplet size of Nano-HO was 23.30 ± 0.46 nm with PDI of 0.087 ± 0.00 (n = 3), and the average zeta potential of Nano-HO was − 6.19 ± 1.70 mV (n = 3). As shown in Fig. 1D, the morphology of Nano-HO was observed by TEM, and it displayed that most microemulsion droplets were nearly spherical with a small size and dispersed homogeneously in aqueous medium. Additionally, Fig. 1E showed that Nano-HO was a transparent viscous liquid at room temperature (a) and formed a clear and transparent microemulsion after diluting with 100-fold distilled water (b). When the same content of HO was suspended in 0.5% CMC-Na solution, it was white turbid liquid (c). All these findings indicated that Nano-HO could significantly increase the solubility of HO in water.

In vitro **drug release**

The *in vitro* release of Nano-HO and HO were dialyzed against PBS (pH 7.4) at 37 °C (Fig. 2A). The contents of HO in the dialysis buffer were quantified by HPLC with a C18 column while a standard curve was made for titration. The results demonstrated that HO and Nano-HO were gradually released into the dialysis buffer over a period of 24 h. The accumulative release rate of Nano-HO (86.3%) was farther than that of regular HO (27.0%) ($p < 0.01$).

Pharmacokinetics study

The mean plasma concentration-time curve profiles after administration with Nano-HO and HO was presented in Fig. 2B, and the pharmacokinetics parameters acquired by the non-compartmental analysis were listed in Fig. 2C. The results demonstrated that the T_{max} was similar in Nano-HO (0.78 ± 0.05) and HO (0.80 ± 0.07). The half-life ($t_{1/2}$) of Nano-HO (1.63 ± 0.31) was prolonged about 1.50-fold as compared to that of HO (1.09 ± 0.22). Moreover, the peak concentration (C_{max}) of Nano-HO (0.78 ± 0.09 μg/mL) was enhanced nearly 1.77-fold than that of HO (0.44 ± 0.02 μg/mL) ($p < 0.01$). The mean residence time (MRT_{0-12}) of Nano-HO (2.83 ± 0.15 h) was slightly longer than that of the HO (2.58 ± 0.10 h). The area under the concentration-time curves from 0 to 12 h (AUC_{0-12} h) of Nano-HO and HO were 2.20 ± 0.06 μg·h/ mL and 1.18 ± 0.05 μg·h/ mL, respectively, yielding a relative bioavailability of 186.44% ($p < 0.01$) for Nano-HO. These findings indicated that when given the same content, Nano-HO could effectively improve the oral bioavailability of HO and prolonged its circulation time in rats.

Nano-HO and HO improved cognitive deficits in TgCRND8 mice

The spatial learning and memory functions of mice was assessed using MWMT. In the training trials, all groups were trained to seek the hidden platform and gradually shortened their escape latency to reach the platform. As shown in Fig. 3B, a significant difference was found in the mean latency between training days ($F(3, 160) = 40.80$, $p < 0.001$) and between treatments ($F(4, 160) = 7.319$, $p < 0.001$), but no

interaction was observed between training day and treatment ($F(12, 160) = 0.3841$, $p > 0.05$). However, mice in Tg + vehicle group exhibited prolonged escape latency compared with WT mice from day 3 ($F(4, 40) = 2.234$, $p < 0.05$) and day 4 ($F(4, 40) = 2.262$, $p < 0.05$). As shown in Fig. 3C-D, TgCRND8 mice stayed less time in the target quadrant ($F(4, 40) = 7.139$, $p < 0.001$) and crossed through the hidden platform with fewer frequency ($F(4, 40) = 8.340$, $p < 0.001$) than WT mice in the probe test. Mice in the HO and Nano-HO groups spent more time in the target quadrant ($p < 0.05$ and $p < 0.01$ respectively) and increased the frequency of crossing platform ($p < 0.05$ for both) when compared to the vehicle-treated TgCRND8 mice. After treatment with donepezil (5 mg/kg), the frequency of crossing platform was higher ($p < 0.05$) and the time spent in the target quadrant longer ($p < 0.05$) than those in the Tg + vehicle group.

Nano-HO and HO decreased the levels of inflammatory cytokines

As shown in Fig. 4, the protein levels of TNF-α ($F(4, 25) = 20.59$, $p < 0.001$), IL-1β ($F(4, 25) = 8.208$, $p < 0.001$) and IL-6 ($F(4, 25) = 18.46$, $p < 0.001$) in the brain tissues of TgCRND8 mice were markedly increased, as compared with the WT group. Treatment with HO and Nano-HO significantly suppressed the productions of TNF-α ($p < 0.01$ for both), IL-1β ($p < 0.01$ and $p < 0.05$, respectively) and IL-6 ($p < 0.01$ for both) in the brain tissues of TgCRND8 mice, as compared with the Tg + vehicle group. Treatment with donepezil (5 mg/kg) could also markedly suppress the protein levels of TNF-α ($p < 0.01$), IL-1β ($p < 0.01$) and IL-6 ($p < 0.01$) in the brain tissues of TgCRND8 mice, as compared with the Tg + vehicle group.

Nano-HO and HO reduced Aβ deposition and inhibited Aβ plaque-associated neuroinflammation

As shown in Fig. 5A, significant increase in the microglia density was observed in the hippocampus ($F(4, 10) = 44.88$, $p < 0.001$) and the cortex ($F(4, 10) = 71.58$, $p < 0.001$) of TgCRND8 mice, as compared with the WT group. Treatment with HO and Nano-HO markedly decreased the microglia density both in the hippocampus ($p < 0.01$ for both) and cortex ($p < 0.01$ for both) of TgCRND8 mice, as compared with the Tg + vehicle group. In addition, there were also marked increase in the astrocyte density in the hippocampus ($F(4, 10) = 41.04$, $p < 0.001$) and cortex ($F(4, 10) = 80.69$, $p < 0.001$) in TgCRND8 mice, when compared with the WT group (Fig. 5B). The HO and Nano-HO treatment significantly attenuated the astrocyte density both in the hippocampus ($p < 0.01$ for both) and cortex ($p < 0.05$ and $p < 0.01$, respectively), as compared with the Tg + vehicle group. Furthermore, as shown in Fig. 5C, Aβ plaque burdens were significantly elevated in the hippocampus ($F(4, 10) = 109.6$, $p < 0.001$) and the cortex ($F(4, 10) = 84.75$, $p < 0.001$) of TgCRND8 mice, as compared with the WT mice. The Aβ plaque burdens in the HO and Nano-HO groups significantly decreased in the hippocampus ($p < 0.05$ and $p < 0.01$ respectively) and the cortex ($p < 0.01$ for both), as compared with the Tg + vehicle group. Donepezil (5 mg/kg) significantly inhibited the microglia and astrocytes infiltration, and also attenuated the Aβ plaque burden in the hippocampus ($p < 0.01$) and the cortex ($p < 0.01$) of TgCRND8 mice. Interestingly, Nano-HO more

markedly decreased the astrocyte density both in the hippocampus ($p < 0.01$) and the cortex ($p < 0.01$), and reduced the Aβ plaque burdens in the hippocampus ($p < 0.05$) of TgCRND8 mice than the HO group.

Nano-HO and HO modulated the APP processing and APP phosphorylation

As shown in Fig. 6, the protein expressions of CTFs ($F(4, 10) = 24.13$, $p < 0.001$), p-APP (Thr 688) ($F(4, 10) = 36.14$, $p < 0.001$), BACE-1 ($F(4, 10) = 46.70$, $p < 0.001$), APH-1 ($F(4, 10) = 19.46$, $p < 0.001$) and PS-1 ($F(4, 10) = 80.72$, $p < 0.001$) in the brain tissues of TgCRND8 mice were significantly augmented, as compared to the WT group. While the protein expressions of IDE ($F(4, 10) = 37.86$, $p < 0.001$) and NEP ($F(4, 10) = 21.74$, $p < 0.001$) were markedly reduced in the brain tissues of TgCRND8 mice, when compared to the WT group. Treatment with HO and Nano-HO significantly mitigated the protein expressions of p-APP (Thr 688) ($p < 0.05$ and $p < 0.01$, respectively), BACE-1 ($p < 0.01$ for both), APH- 1 ($p < 0.01$ for both) and PS-1 ($p < 0.01$ for both) in the brain tissues of TgCRND8 mice, when compared with the Tg + vehicle group. In addition, Nano-HO significantly increased the protein expressions of IDE ($p < 0.01$) and NEP ($p < 0.01$) in the brain tissues of TgCRND8 mice, while HO treatment did not affect the protein expressions of IDE and NEP in the brain tissues of TgCRND8 mice, when compared with the Tg + vehicle group. Treatment with donepezil (5 mg/kg) also markedly suppressed the protein expressions of p-APP (Thr 688) and PS-1 ($p < 0.01$), while obviously enhanced the protein expressions of IDE ($p < 0.01$) and NEP ($p < 0.01$) in the brain tissues of TgCRND8 mice, when compared with the Tg + vehicle group. Interestingly, Nano-HO was more effective than HO in inhibiting the protein expressions of p-APP ($p < 0.05$) and BACE-1 ($p < 0.01$), as well as enhancing the protein expressions of IDE ($p < 0.01$) and NEP ($p < 0.01$) in the brain tissues of TgCRND8 mice.

The above results demonstrated that Nano-HO could significantly inhibit the expression of BACE-1. Thus, a molecular docking of HO with BACE-1 was conducted to investigate whether HO was a BACE-1 inhibitor. The molecular docking results showed that HO could form three hydrogen bonds at specific residues (Lys107, Asp216 and VAL170) with BACE-1 protein with binding energy of -6.64, -6.75, -6.85 kcal/mol, respectively, and with bond lengths of 2.503 Å, 2.382 Å and 2.215 Å, respectively (Fig. 6E). The docking results were consistent with the above western blot data, indicating that HO is a BACE-1 inhibitor.

Nano-HO and HO suppressed apoptosis and tau protein hyperphosphorylation

The protein level of caspase-3 ($F(4, 10) = 44.72$, $p < 0.001$) in the brain tissues of TgCRND8 was significantly elevated, while Bcl-2 expression ($F(4, 10) = 7.979$, $p < 0.01$) was decreased, when compared with the WT group (Fig. 7A-B, respectively). After treatment with HO, Nano-HO and donepezil, the expressions of caspase-3 were effectively mitigated ($p < 0.01$ for all). In addition, Nano-HO and donepezil treatment also significantly increased the Bcl-2 expression ($p < 0.01$ for both), when compared with the Tg + vehicle group.

Moreover, as shown in Fig. 7C-D, the ratio of p-Tau (Thr 205)/tau (46) ($F(4, 10) = 65.18$, $p < 0.001$) and p-Tau (Ser 404)/tau (46) ($F(4, 10) = 5.266$, $p < 0.05$) was markedly increased in the brain tissues of TgCRND8 mice. Treatment with HO and Nano-HO significantly down-regulated the ratio of p-Tau (Thr 205)/tau (46) ($p < 0.01$ for both). Nano-HO markedly decreased the ratio of p-Tau (Ser 404)/tau (46) ($p < 0.05$) as compared with the Tg + vehicle group. Donepezil treatment obviously reduced the ratios of p-Tau (Thr 205)/tau (46) and p-Tau (Ser 404)/tau (46) ($p < 0.01$ for both). However, no significant differences were found among all groups in the expressions of p-Tau (Ser 396) ($F(4, 10) = 2.142$, $p > 0.05$). Notably, Nano-HO was more effective than HO in inhibiting the protein expressions of p-Tau (Thr 205)/tau (46) ($p < 0.01$).

Nano-HO and HO regulated the JNK/CDK5/GSK-3β signaling pathway

As clearly shown in Fig. 8, as compared to the WT group, the ratio of p-JNK/JNK was notably up-regulated in the Tg + vehicle group ($F(4, 10) = 46.49$, $p < 0.001$). HO and Nano-HO treatments was able to down-regulate the ratio of p-JNK/JNK ($p < 0.01$ for both), as compared with the Tg + vehicle group. Additionally, significant increase in the ratio of p-35/CDK5 ($F(4, 10) = 17.71$, $p < 0.001$) was observed in the Tg + vehicle group as compared to WT group, which was remarkably attenuated by HO and Nano-HO treatment ($p < 0.05$ and $p < 0.01$, respectively). On the other hand, the ratio of p-GSK-3β (Ser9)/GSK-3β were markedly decreased in the brain tissues of TgCRND8 mice ($F(4, 10) = 36.44$, $p < 0.001$), as compared with the WT group. Treatment with HO and Nano-HO obviously increased the ratio of p-GSK-3β (Ser9)/GSK-3β ($p < 0.01$ for both). Treatment with donepezil (5 mg/kg) significantly decreased the ratio of p-35/CDK5 ($p < 0.01$) and recovered the ratio of p-GSK-3β (Ser9)/GSK-3β ($p < 0.01$). On the other hand, Nano-HO showed more potency in inhibiting the activation of GSK-3β via elevating the ratio of p-GSK-3β (Ser9)/GSK-3β ($p < 0.05$) than regular HO.

Differences in gut microbiota profile among WT, Tg and HO treatment groups

The system clustering tree (Fig. 9A) revealed significant differences among five groups. Samples in HO and Nano-HO groups were clustered separately from Tg + vehicle group, reflecting that HO and Nano-HO prevented the changes of gut microbiota in TgCRND8 mice.

For the α-diversity analysis, the Shannon index was significantly decreased ($F(4, 25) = 3.96$, $p < 0.05$) and Simpson index was remarkably increased ($F(4, 25) = 8.887$, $p < 0.001$) in TgCRND8 mice (Fig. 9B-C). Nano-HO and HO treatments improved the Shannon index although the improvement failed to reach a significant difference ($p > 0.05$ for both), while the treatment significantly decreased the Simpson index ($p < 0.05$, $p < 0.01$ respectively), indicating that Nano-HO and HO could improve the diversity and species evenness in the fecal samples of TgCRND8 mice.

In addition, principal coordinate analysis (PCoA) and partial least squares discrimination analysis (PLS-DA) both yielded well separated positions among the groups (Fig. 9D-E). Notably, the bacterial communities in the Nano-HO group were more closely clustered with the WT mice than HO group, which differed from TgCRND8 mice, suggesting that the bacterial communities in TgCRND8 mice were changed and the gut microbiota composition differed among the five groups.

Gut microbiota composition at different levels among five experimental groups

Figure 10 and Fig. 11 illustrated the gut microbiota community composition and dominant bacterial distribution at different levels in fecal samples.

At the phylum level, the most abundant phyla were *Bacteroidetes, Firmicutes, Proteobacteria*, accounting for 90% of the total microbiome composition, followed by *Cyanobacteria-1*, *Deferribacteria* and *Actinobacteria* (Fig. 10A, Fig. 11A). As shown in Fig. 11A, the relative abundance of *Firmicutes* was decreased by 59.0% ($F(4, 25) = 9.712$, $p < 0.001$), but *Bacteroidetes* and *Proteobacteria* were increased by 186.6% ($F(4, 25) = 10.36$, $p < 0.001$) and 278.0% ($F(4, 25) = 16.47$, $p < 0.001$), respectively, in the Tg + vehicle group, when comparing to the WT group. Nano-HO exerted similar effect as HO on reversing the proportions of *Firmicutes, Bacteroidetes* and *Proteobacteria* in TgCRND8 mice, but had better effect than HO on returning the proportions of *Deferribacteria* and *Actinobacteria* in TgCRND8 mice, as compare with the Tg + vehicle group.

At the class level, a total of 16 genera were identified in all samples (Fig. 10B). As shown in Fig. 11B, the relative abundance of *Bacillus* ($F(4, 25) = 18.76$, $p < 0.001$), *α-Proteobacteria* ($F(4, 25) = 23.57$, $p < 0.001$), *β-Proteobacteria* ($F(4, 25) = 13.14$, $p < 0.010$), *δ-Proteobacteria* ($F(4, 25) = 11.07$, $p < 0.001$) and *ε-Proteobacteria* ($F(4, 25) = 66.63$, $p < 0.001$) were significant higher in TgCRND8 mice, as compared to the WT group. However, the relative abundance of *Erysipelotrichi* was significantly lower ($F(4, 25) = 5.996$, $p < 0.01$) in the Tg + vehicle group. Nano-HO exerted similar inhibitory effect to HO on the relative abundance of *Bacillus, β-Proteobacteria* and *δ-Proteobacteria*, but has powerful reversion effect than HO on the proportions of *Erysipelotrichi, ε-Proteobacteria* and *α-Proteobacteria* in TgCRND8 mice, as compare with the Tg + vehicle group.

At the order level, a total of 19 genera were identified in all samples (Fig. 10C). As shown in Fig. 11C, *Clostridiales* was of predominance in all samples among five groups and showed a high abundance in the Tg + vehicle group ($F(4, 25) = 9.757$, $p < 0.001$). The relative abundances of *Campylobacterales* ($F(4, 25) = 25.07$, $p < 0.001$) and *Desulfovibrionales* ($F(4, 25) = 25.64$, $p < 0.01$) were significantly higher in TgCRND8 mice, whereas the relative abundances of *YS32* ($F(4, 25) = 20.63$, $p < 0.001$) and *Bifidobacteriales* ($F(4, 25) = 6.76$, $p < 0.001$) remarkably decreased in TgCRND8 mice, as compared with the WT group. The proportion of *Turcibacterales* was decreased in TgCRND8 mice but failed to show a difference ($F(4, 25) = 1.538$, $p > 0.05$), as compared with the WT group. Nano-HO exerted similar inhibitory effect to HO on the relative abundance of *Clostridiales, Campylobacterales* and *Desulfovibrionales*, but

had better enhancement effect than HO on the relative abundance of *YS32* and *Bifidobacteriales* in TgCRND8 mice, as compare with the Tg + vehicle group.

At the family level, totally 23 genera were identified in all samples (Fig. 10D). As shown in Fig. 11D, the proportion of *S24-7* was significantly decreased ($F(4, 25) = 12.06$, $p < 0.001$), but the proportions of *Ruminococcaceae* ($F(4, 25) = 9.894$, $p < 0.001$), *Lachbaccillace* ($F(4, 25) = 17.18$, $p < 0.001$), *Helicobacteraceae* ($F(4, 25) = 39.54$, $p < 0.001$), *Odoribacteraceae* ($F(4, 25) = 12.30$, $p < 0.001$) and *Prevotellaceae* ($F(4, 25) = 3.971$, $p < 0.01$) were markedly increased in TgCRND8 mice, as compared to the WT group. Nano-HO produced similar effect to HO on the relative abundance of *S24-7, Ruminococcaceae, Lachbaccillace* and *Prevotellaceae*, but had better inhibitory effect than HO on the relative abundance of *Helicobacteraceae* and *Odoribacteraceae* in TgCRND8 mice, as compare with the Tg + vehicle group.

Finally, a total of 22 genera were identified in all samples (Fig. 10E). As shown in Fig. 11E, the relative abundances of *Akkermansia* ($F(4, 25) = 8.778$, $p < 0.001$), *Lactobacillus* ($F(4, 25) = 7.718$, $p < 0.001$) and *Parabacteroides* ($F(4, 25) = 4.999$, $p < 0.01$) were significant lower in TgCRND8 mice, as compared with the WT group. In contrast, the proportions of *Allobaculum* ($F(4, 25) = 8.119$, $p < 0.001$), *Mucispirillum* ($F(4, 25) = 16.61$, $p < 0.001$) and *Oscillospira* ($F(4, 25) = 12.30$, $p < 0.001$) were higher in TgCRND8 mice, as compared with the WT group. Nano-HO had equal efficacy as HO on reducing the relative abundances of *Akkermansia*, *Allobaculum*, *Lactobacillus*, *Oscillospira, Mucispirillum* and *Parabacteroides* in TgCRND8 mice, as compare with the Tg + vehicle group.

Discussion

HO has been reported to improve cognitive deficits in several animal models of AD via clearing Aβ deposition, inhibiting AChE activity and suppressing neuroinflammation [14, 16, 17, 37, 38], but the poor water solubility badly limited its bioavailability and potential medicinal application. Nano-DDS is beneficial for prolonging exposure time, increasing drug efficacy and overcoming poor bioavailability of drugs, which makes it appealing as a universal vehicle for lipophilic drugs. It is well-known that droplet size of nanoparticles (10–50 nm) is a critical factor since it is closely associated with the rate, extent and absorption of drug release. Our results showed that Nano-HO could form nano-sized microemulsion droplets (23.30 ± 0.46 nm) when diluted with distilled water (Fig. 1B). Meanwhile, low PDI reflects the uniformity of particle size. The closer the PDI value is to zero, the more homogeneous the droplets are [39]. Additionally, stability of nanoparticles partially depends on the surface zeta potential, a parameter that gives the magnitude of the electrostatic repulsive interactions between particles [40]. A higher value of zeta potential usually hinders the probability of coalescence, thereby maintaining homogeneity of droplet size [41]. Our results indicated that Nano-HO formulation exhibited a relatively high negative average zeta potential and a low PDI value, suggesting that it met the required zeta potential prerequisite for a stable microemulsion. In addition, the accumulative release rate of HO from Nano-HO (86.3%) in PBS (pH 7.4) was significantly higher than that from regular HO (27.0%) over a period of 24 h (Fig. 2A). Possible reasons may include that small droplet size of Nano-HO provided a large surface area for drug release into the aqueous phase. On the other hand, the pharmacokinetics study was investigated in rats

to compare the bioavailability of Nano-HO with that of regular HO. The results demonstrated that the $t_{1/2}$ and MRT_{0-12} were both prolonged in Nano-HO group than in the regular HO group, suggesting that the oral bioavailability of Nano-HO was greatly improved as compared with regular suspension. Moreover, the AUC_{0-12} h of Nano-HO (2.20 ± 0.06 μg·h/ mL) was significantly increased when compared with HO (1.18 ± 0.05 μg·h/ mL), resulting in a relative bioavailability of 186.44% to HO. These findings indicated that the improved bioavailability of Nano-HO was predominantly owing to the increased solubility. Moreover, Nano-HO exerted better improving effects on cognitive deficits in TgCRND8 mice than HO, and these findings were believed to be related to the improved oral bioavailability of Nano-HO.

Neuroinflammation is widely considered as one of the major pathological factors of AD. Microglias are the primary inflammatory cells in the brain. Astrocytes, the most abundant glial subtype in the central nervous system, also play a critical role in the pathogenesis of AD. Growing lines of evidence have demonstrated that Aβ accumulation in AD causes microglia activation and astrocyte recruitment, thereby inducing the release of pro-inflammatory cytokines including TNF-α, IL-6 and IL-1β [42–44]. Meanwhile, inflammation could induce the expression of BACE-1, promote Aβ deposition, and exacerbate tau protein hyperphosphorylation and neurons loss. Therefore, inflammation is the core driver of AD pathogenesis. In this study, we found that both Nano-HO and regular HO could prevent the microgliosis, astrogliosis and Aβ deposits in the hippocampus and cortex of TgCRND8 mice, as well as suppress the release of TNF-α, IL-1β and IL-6 in the brain tissues of TgCRND8 mice (Fig. 4 and Fig. 5). Interestingly, Nano-HO inhibited astrogliosis in both hippocampus and cortex of TgCRND8 mice in a more potent manner than HO (Fig. 5B). These findings indicated that the amelioration of Nano-HO on hippocampal-dependent memory function was attributable to its anti-inflammatory property.

It is well-known that Aβ deposition is a key pathogenic hallmark in AD pathogenesis. Increased production of Aβ peptides and formation of Aβ plaques through sequential cleavage of APP by the β- and γ-secretases contribute to the pathological basis of AD [45]. Specifically, p-APP (Thr 668), as observed near the plaques, may increase the Aβ levels by facilitating the exposure and cleavage by β-secretase BACE-1 [46]. PS-1 and APH-1 are vital catalytic submits of γ-secretase responsible for APP cleavage to Aβ [47, 48]. Increasing evidence revealed that proteolytic degradation is a particularly important determinant of cerebral Aβ levels, and Aβ-degrading enzymes including IDE and NEP play critical roles in Aβ degradation [49]. Therefore, inhibition of β- or γ-secretase or enhancement of Aβ-degrading enzymes could help to reduce the Aβ production. Our results demonstrated that Nano-HO showed similar effect in inhibiting the protein expressions of APH-1 and PS-1 as HO (Fig. 6). Interestingly, Nano-HO showed better effect on inhibiting the protein expressions of p-APP (Thr 688) and BACE-1, and enhancing the protein expressions of IDE and NEP than that of HO. These results suggested that Nano-HO may modulate APP processing and phosphorylation through suppressing the activities of β- and γ-secretases and enhancing the activities of Aβ-degrading enzymes to clear the Aβ deposition in the brains of TgCRND8 mice. Furthermore, our molecular docking results demonstrated that HO was well docked with BACE-1 at three active sites including Lys 107, Asp 216 and VAL 170 (Fig. 6E), suggesting that HO may be a BACE-1 inhibitor.

Abnormally high level of hyperphosphorylated tau protein is another typical pathological hallmark of AD, which also leads to oxidative stress via increasing the reactive oxygen species (ROS) production. Increased ROS could promote inflammatory response, then induce neuronal apoptosis or loss, ultimately resulting in learning and memory impairments [50, 51]. It has been reported that the phosphorylation of tau protein is abnormally accentuated at different sites of Thr 205 (7.61 times increase), Ser 396 (4.95 times increase) and Ser 404 (2.97 times increase) in the postmortem brain tissues of AD patients [52]. In addition, up-regulation of caspase-3 is directly responsible for cellular apoptosis in AD [53]. Thus, inhibition of tau protein hyperphosphorylation and neuronal apoptosis may be potential therapeutic targets for AD. Our results revealed that Nano-HO could inhibit tau protein hyperphosphorylation at Thr 205 and Ser 404 sites, as well as the protein expression of caspase-3, but enhance the protein expression of Bcl-2 in the brain tissues of TgCRND8 mice (Fig. 7), indicating that the inhibitory effect of Nano-HO on specific hyperphosphorylation of tau protein and apoptosis may be the underlying molecular mechanisms of its cognitive function improving effects.

Activation of JNK pathway has been consistently found in the surrounding area of the Aβ plaques in AD patients and transgenic mice via facilitating p-APP (Thr 668) in culture cell lines [54–56] and exaggerating p-tau (Thr 205) [57]. In our present study, both Nano-HO and HO significantly down-regulated the ratio of protein expressions of p-JNK/JNK in brain tissues of TgCRND8 mice (Fig. 8A). In addition, JNK pathway is also closely involved in the activation of GSK-3β, which is considered to be a key kinase responsible for APP phosphorylation in neuronal cells and intimately associated with AD progression [58, 59]. Hyperactivation of GSK-3β has been found in the brains of AD patients [60]. Suppressing GSK-3β activity has been demonstrated to decrease the generation and accumulation of Aβ in APP transgenic mice of AD [61]. Moreover, GSK-3β is also a major kinase associated with the aberrant phosphorylation of tau [62], which could be inactivated by phosphorylation at Ser 9 site, suggesting that agents with ability to up-regulate p-GSK-3β (Ser 9) maybe potential candidates for the treatment or prevention of AD [63, 64]. Our results indicated that Nano-HO had better efficacy than HO on enhancing the ratio of p-GSK-3β (Ser9)/GSK-3β in the brain tissues of TgCRND8 mice (Fig. 8C).

Meanwhile, CDK5 plays a crucial role in the development of central nerve system and AD progression [65]. Under pathological conditions, CDK5 was activated via direct binding to its neuronal specific activators p-35, and then aggravate tau hyperphosphorylation by enhancing GSK-3β, exacerbate neuronal loss and subsequently lead to neurodegeneration [66–71]. Therefore, agents that suppress the CDK5 activity may ameliorate plaque pathology, neurofibrillary and neuronal loss in AD. Our results indicated that Nano-HO suppressed the ratio of p-35/CDK5 in the brain tissues of TgCRND8 mice, suggesting that the cognitive deficits improving effects of Nano-HO were associated with its ability to inhibit the CDK5 activity, and the finding was also consistent with the improvement on kinase activity GSK-3β of Nano-HO.

The bacteria community in the gut can directly reflect the health status of the host by maintaining a certain proportion to protect the bacterial flora balance. The changes in bacterial diversity and richness can lead to the dysfunctions of the bacterial community, and trigger brain-gut axis dysbiosis, contributing to the occurrence of neurodegenerative disorders like AD [72]. In our study, the decreased Shannon index

and increased Simpson index suggested that TgCRND8 mice were associated with the diversity and evenness deduction of the bacterial community, as compared with the WT mice (Fig. 9B-C), and the observation was consistent with the similar decline of bacterial diversity in AD patients [73, 74]. The structural variability or similarity among different treatment groups was assessed by system clustering tree, PCA and PLS-DA in our study (Fig. 9B and 9E-F). These results showed that the mice in Nano-HO group clumped visibly far away from the TgCRND8 mice, emphasizing that the bacteria community tended to recover to normal. This observation was consistent with the finding of the changed intestinal bacteria in AD patients as reported before [75].

Several studies have demonstrated an essential role of gastrointestinal microbes in the development of cerebral Aβ amyloidosis along with a peripheral inflammatory state [76, 77]. Bacteria living in the intestinal tract adhere to the intestinal mucosal surface of epithelial cells, forming bacterial flora, thereby affecting the intestinal integrity and permeability [78]. When the harmful bacteria destroyed the integrity of intestinal epithelial cells, the inflammatory reaction was triggered or aggravated accompanied with an increase in inflammatory cytokine (e.g., IL-6 and TNF-α) levels [79]. Our study showed that the bacterial community altered, which coincided with the productions of TNF-α, IL-1β and IL-6, along with increase of Aβ plaques in brains. These results implied that TgCRND8 mice might cause the damage of the brain via changing the bacteria condition in the gut.

Reduction of given beneficial bacteria increased the inflammation, which can be harmful to the intestinal structure. Such reduction can be characterized in *Firmicutes spp.* and *Bifidobacteria spp.* [80–82]. Metabolites secreted by *Firmicutes spp.* decreased the production of pro-inflammatory factors such as TNF-α, thus suppressed the occurrence of inflammation [83]. Probiotics such as *Lactobacillales spp.* and *Bifidobacteriales spp.* improved the conditions of inflammation and intestinal epithelial barrier function impairment [80, 82]. In AD mouse model, acetate (a metabolite of *Bifidobacterium breve* strain A1) has been reported to ameliorate cognitive disturbances [84]. It is worth noting that when compared to the WT mice (53.6%, in phylum level, 1.18% in order level, and 2.61% in genus level,), there was a decline of *Firmicutes, Bifidobacteria* and *Lactobacillus* by 42.4%, 87.3%, and 69.7%, respectively, in TgCRND8 mice (Fig. 11A, C and E), revealing that the reduction of beneficial bacteria was a potential cause of intestinal inflammation in TgCRND8 mice.

Additionally, fewer *Actinobacteria*, but more *Bacteroidetes* and *Proteobacteria* were found in the intestinal microbiota of AD patients or APP/PS1 transgenic mice when compared to healthy controls [74, 77], suggesting that bacterial dysbiosis was positively associated with the progression of AD. In our study, we noticed that the relative abundance of *Firmicutes, Proteobacteria* and *Bacteroidetes* were major community at the phylum level, which account to almost 90%, followed by *Actinobacteria* and *Cyanobacteria*. The relative abundance of *Actinobacteria* had an 88% decrease in TgCRND8 mice, as compared with the WT mice, while the proportion of the *Proteobacteria*, *Bacteroidetes* and *Cyanobacteria* visibly increased by 235.3%, 99.7% and 125% respectively in TgCRND8 mice, as compared to the WT mice. Those alterations were in accordance with the previous reports [85, 86]. Nano-HO inhibited the relative abundance of the *Firmicutes*, *Proteobacteria*, *Bacteroidetes* and *Cyanobacteria* in TgCRND8 mice

as similar to that of regular HO. Interestingly, Nano-HO enhanced the relative abundance of *Actinobacteria* in TgCRND8 mice in a more potent manner than HO (Fig. 11A).

Recently, the effect of chronic *Helicobacter pylori* infection on AD has been demonstrated by the release of massive inflammatory mediators [87]. *Helicobacter pylori* filtrate could cause tau protein hyperphosphorylation in mouse neuroblastoma N2a cells and brains of rats via activation of GSK-3β [88]. Our results demonstrated that the relative abundance of *Helicobacteraceae* (at family level, Fig. 11D) in TgCRND8 group was augmented by 532.3% as compared to the WT group. Interestingly, Nano-HO reversed this change in TgCRND8 mice in a more potent manner than HO.

Mucin-degrading bacteria are identified as microbial drivers. Among them, *Prevotella* degrades mucin and *Desulfovibrio* enhances the rate-limiting sulfatase step by hydrolyzing glycosyl sulfate esters. *Ruminococcus* is also able to degrade mucins [89]. As probiotics strains, *Akkermansia* can secrete immunoglobulin A (IgA) and antibacterial peptides by immunological rejection to resist pathogen damage to the intestine, thereby possessing anti-inflammatory and barrier-improving properties [90, 91]. Our results showed that the relative abundance of *Desulfovibrionales* (at order level, Fig. 11C), *Prevotellaceae* (at family level, Fig. 11D) and *Ruminococcaceae* (at family level, Fig. 11D) drastically increased to 457.6%, 325.6% and 139.3%, respectively, in TgCRND8 mice, as compared with the WT group, and the changes may be of relevance to the increased transmembrane permeability. The relative abundance of *Akkermansia* (at genus level, Fig. 11E) significantly decreased in TgCRND8 group, as compared with the WT group. Nano-HO and HO reversed these changes in TgCRND8 mice. Figure 12 schematically summarized the molecular mechanisms underlying the cognitive deficits ameliorating actions of Nano-HO and HO in TgCRND8 mice.

Conclusions

Our study demonstrated for the first time that Nano-HO could improve cognitive deficits in a more potent manner than HO in TgCRND8 mice via inhibiting the infiltration of astrogliosis and β-secretase, upregulating Aβ-degrading enzymes, suppressing tau protein hyperphosphorylation at site Thr 205, inhibiting JNK pathway and activating GSK-3β pathway. The multi-target effects of Nano-HO against cognitive deficits in TgCRND8 mice were mediated, at least in part, via inhibiting neuroinflammation and tau hyperphosphorylation, modulating APP processing and phosphorylation through suppressing the activation of JNK/CDK5/GSK-3β signaling pathway. Furthermore, Nano-HO could regulate the compositions and structures of gut microbiota to protect the gut microflora and its stability. Taken together, Nano-HO is a promising Nano-based formulation with natural compound worthy of further development into AD treatment.

Abbreviations

AD

Alzheimer's disease; Aβ:β-amyloid; APH-1:anterior pharynx-defective-1; APP:amyloid precursor protein; BACE-1:β-site APP cleaving enzyme-1; Bcl-2:B cell lymphoma-2; CDK5:cyclin-dependent kinase 5; CMC-Na:sodium carboxymethylcellulose; GSK-3β:glycogen synthase kinase 3β; HO:Honokiol; HPLC:high performance liquid chromatography; IDE:insulin degrading enzyme; IL-6:interleukin 6; IL-1β:interleukin 1β; PS-1:presenilin-1; JNK:c-Jun N-terminal kinase; MCT:Medium-chain triglycerides; MWMT:Morris Water Maze test; Nano-HO:honokiol nanoscale drug delivery system; NEP:neprilysin; NFTs:neurofibrillary tangles; PBS:phosphate-buffered saline; PDI:poly-dispersity index; TEM:transmission electron microscope; TNF-α:tumor necrosis factor; WT:wild type; ZP:zeta potential.

Declarations

Ethics approval and consent to participate

All experimental procedures were conducted in accordance with the guidelines for animal research of The Chinese University of Hong Kongand were approved by the Animal Experimentation Ethics Committee of The Chinese University of Hong Kong(Ref. No. 18/108/GRF).

Consent for publication

All authors have consented for publication.

Availability of data and materials

All the primary data supporting the conclusions of this study are availablefrom the corresponding author on a reasonable request.

Competing interests

The authors declare no conflicts of interest with respect to this article.

Funding

This work was supported by Natural Science Foundation of Guangdong Province of China(project no. 2019A1515011257), the CUHK Direct Grant (project no. 2017.076)andNatural Science Foundation of China (project no. 81973519).

Authors' contribution

XYF and LZXconceived the research idea and designed the experimental protocols. QC performed the animal experiments andcollected the experimental data.LQP analyzed the HPLC data. SZR provided and authenticated HO. ISP performed the data analysis.YQJ supervised the IHC staining. XQQ helped the animal experiments and checked the references.YW conducted the molecular docking.HYF prepared the Nano-HO formulation.QCdrafted the manuscript. XYF and LZX revised the manuscript.All authors read and approved the final manuscript.

Acknowledgements

Not applicable.

References

1. Gee MS, Son SH, Jeon SH, Do J, Kim N, Ju YJ, et al. A selective p38α/β MAPK inhibitor alleviates neuropathology and cognitive impairment, and modulates microglia function in 5XFAD mouse. Alzheimers Res Ther. 2020;12:45.
2. Hamm V, Heraud C, Bott JB, Herbeaux K, Strittmatter C, Mathis C, et al. Differential contribution of APP metabolites to early cognitive deficits in a TgCRND8 mouse model of Alzheimer's disease. Sci Adv. 2017;3:e1601068.
3. Palop JJ, Mucke L. Amyloid-β-induced neuronal dysfunction in Alzheimer's disease: from synapses toward neural networks. Nat Neurosci. 2010;12:812–8.
4. Selkoe DJ. Cell biology of protein misfolding: The examples of Alzheimer's and Parkinson's diseases. Nat Cell Bio. 2004;4:1054–61.
5. Wilquet V, Strooper BD. Amyloid-beta precursor protein processing in neurodegeneration. Curr Opin Neurobiol. 2004;14:582–8.
6. Tiwari S, Atluri V, Kaushik A, Yndart A, Nair M. Alzheimer's disease: pathogenesis, diagnostics, and therapeutics. Int J Nanomedicine. 2019;14:5541–54.
7. Bossy-Wetzel E, Schwarzenbacher R, Lipton SA. Molecular pathways to neurodegeneration. Nat Med. 2004;10:2–9.
8. Tesco G, Koh YH, Kang EL, Cameron AN, Das S, Sena-Esteves M, et al. Depletion of GGA3 stabilizes BACE and enhances beta-secretase activity. Neuron. 2007;54:721–37.
9. Hampel H, Ewers M, Bürger K. Lithium trial in Alzheimer's disease: a randomized, single-blind, placebo-controlled, multicenter 10-week study. J Clin Psychiat. 2009;70:922–31.
10. Egan MF, Kost J, Tariot PN. Randomized trial of verubecestat for mild-to-moderate Alzheimer's disease. N Engl J Med. 2018;378:1691–703.
11. Honig LS, Vellas B, Woodward M. Trial of solanezumab for mild dementia due to Alzheimer's disease. N Engl J Med. 2018;378:321–30.
12. Howes MJ, Perry E. The role of phytochemicals in the treatment and prevention of dementia. Drugs Aging. 2011;28:439–68.
13. Cui HS, Huang LS, Sok DE, Shin J, Kwon BM, Youn UJ, et al. Protective action of honokiol, administered orally, against oxidative stress in brain of mice challenged with NMDA. Phytomedicine. 2017;14:696–700.
14. Zhang P, Liu XY, Zhu YJ, Chen SZ, Zhou DM, Wang YY. Honokiol inhibits the inflammatory reaction during cerebral ischemia reperfusion by suppressing NF- kB activation and cytokine production of glial cells. Neurosci Lett. 2013;534:123–7.

15. Matsui N, Takahashi K, Takeichi M, Kuroshita T, Noguchi K, Yamazaki K, et al. Magnolol and honokiol prevent learning and memory impairment and cholinergic deficit in SAMP8 mice. Brain Res. 2009;1305:108–17.
16. Xian YF, Ip SP, Mao QQ, Su ZR, Chen JN, Lai XP, et al. Honokiol improves learning and memory impairments induced by scopolamine in mice. Eur J Pharmacol. 2015;760:88–95.
17. Xian YF, Ip XP, Mao QQ, Lin ZX. Neuroprotective effects of honokiol against beta-amyloid-induced neurotoxicity via GSK-3β and β-catenin signaling pathway in PC12 cells. Neurochem Int. 2016;97:8–14.
18. Wang LJ, Dong JF, Chen J, Eastoe JL, Li XF. Design and optimization of a new self-nanoemulsifying drug delivery system. J Colloid Interface Sci. 2009;330:443–8.
19. Date AA, Desai N, Dixit R, Nagarsenker M. Self-nanoemulsifying drug delivery systems: formulation insights, applications and advances. Nanomedicine. 2010;5:1595–616.
20. Mancuso C, Santangelo R. Alzheimer's disease and gut microbiota modifications: the long way between preclinical studies and clinical evidence. Pharmacol Res. 2017;129:329–36.
21. Schwenger KJP, Bolzon CM, Li C, Allard JP. Non-alcoholic fatty liver disease and obesity: the role of the gut bacteria. Eur J Nutr. 2019;58:1771–84.
22. Vrakas S, Mountzouris KC, Michalopoulos G, Karamanolis G, Papatheodoridis G, Tzathas C, et al. Intestinal bacteria composition and translocation of bacteria in inflammatory Bowel disease. PLoS One. 2017;12:e0170034.
23. Komatsuzaki N, Shima J, Kawamoto S, Momose H, Kimura T. Production of γ-aminobutyric acid (GABA) by Lactobacillus paracasei isolated from traditional fermented foods. Food Microbiol. 2015;22:497–504.
24. Freestone PPE, Haigh RD, Williams PH, Lyte M. Involvement of enterobactin in norepinephrine-mediated iron supply from transferrin to enterohaemorrhagic Escherichia coli. FEMS Microbiol Lett. 2010;222:39–43.
25. Lee YJ, Ba ZY, Roberts RF, Rogers CJ, Fleming JA, Meng HC, et al. Effects of Bifidobacterium animalis subsp. lactis BB-12 on the lipid/lipoprotein profile and short chain fatty acids in healthy young adults: a randomized controlled trial. Nutr J. 2017;16:154–62.
26. Shen HP, Guan QB, Zhang XL, Yuan C, Tan ZY, Zhai LP, et al. New mechanism of neuroinflammation in Alzheimer's disease: The T activation of NLRP3 inflammasome mediated by gut microbiota. Prog Neuro-psychoph. 2020;100:109884.
27. Zhan GF, Yang N, Li S, Huang NN, Fang X, Zhang J, et al. Abnormal gut microbiota composition contributes to cognitive dysfunction in SAMP8 mice. Aging-US. 2018;10:1257–67.
28. Hyde LA, Kazdoba TM, Grilli. Age-progressing cognitive impairments and neuropathology in transgenic CRND8 mice. Behav Brain Res. 2005;160:344–55.
29. Chishti MA, Yang DS, Janus C. Early-onset amyloid deposition and cognitive deficits in transgenic mice expressing a double mutant form of amyloid precursor protein 695. J Biol Chem. 2001;276:21562–70.

30. Durairajan SS, Liu LF, Lu JH. Berberine ameliorates beta-amyloid pathology, gliosis, and cognitive impairment in an Alzheimer's disease transgenic mouse model. Neurobiol Aging. 2012;33:2903–19.
31. Wang X, Wang YQ, Geng YL, Li FW, Zheng CC. Isolation and purification of honokiol and magnolol from cortex Magnoliae officinalis by high-speed counter-current chromatography. J Chromatogr A. 2004;1036:171–5.
32. Xu ZZ, Yang J, Bai J, Bai XY, Wang JC. Preparation and pharmacokinetic study of oral self-microemulsifying delivery systems containing honokiol. Chinese J New Drug. 2012;21:857–62.
33. Li HQ, Ip SP, Yuan QJ, Zheng GQ, Tsim KKW, Dong TTX, et al. Isorhynchophylline ameliorates cognitive impairment via modulating amyloid pathology, tau hyperphosphorylation and neuroinflammation: Studies in a transgenic mouse model of Alzheimer's disease. Brain Behav Immune. 2019;82:264–78.
34. Li HT, Jia JP, Wang W, Hou TT, Tian YRH, Wu QQ, et al. Honokiol Alleviates Cognitive Deficits of Alzheimer's Disease (PS1(V97L)) Transgenic Mice by Activating Mitochondrial SIRT3. J Alzheimers Dis. 2018;64:291–302.
35. Wang DM, Dong XH, Wang CY. Honokiol ameliorates amyloidosis and neuroinflammation and improves cognitive impairment in Alzheimer's disease transgenic mice. J Pharmacol Exp Ther. 2018;366:470–8.
36. Vorhees CV, Williams MT. Morris water maze: procedures for assessing spatial and related forms of learning and memory. Nat Protoc. 2006;1:848–58.
37. Hoi CP, Ho YP, Baum L, Chow AHL. Neuroprotective effect of honokiol and magnolol, compounds from Magnolia officinalis, on beta-amyloid-induced toxicity in PC12 cells. Phytother Res. 2010;24:1538–42.
38. Qiang LQ, Wang CP, Wang FM, Pan Y, Yi LT, Zhang X, et al. Combined administration of the mixture of honokiol and magnolol and ginger oil evokes antidepressant-like synergism in rats. Arch Pharm Res. 2009;32:1281–92.
39. Zhao L, Wei YM, Huang Y, He B, Zhou Y, Fu JJ. Nanoemulsion improves the oral bioavailability of baicalin in rats: in vitro and in vivo evaluation. Int J Nanomedicine. 2013;8:3769–79.
40. Zhou J, Tan L, Xie J, Lai Z, Huang Y, Qu C, et al. Characterization of brusatol self-microemulsifying drug delivery system and its therapeutic effect against dextran sodium sulfate-induced ulcerative colitis in mice. Drug Deliv. 2017;24:1667–79.
41. Zhu Y, Zhang J, Zheng Q, Wang M, Deng W, Li Q, et al. In vitro and in vivo evaluation of capsaicin-loaded microemulsion for enhanced oral bioavailability. J Sci Food Agric. 2014;95:2678–85.
42. Cai ZY, Hussain MD, Yan LJ. Microglia, neuroinflammation, and beta-amyloid protein in Alzheimer's disease. Int J Neurosci. 2014;124:307–21.
43. Akiyama H, Barger S, Barnum S, Bradt B, Bauer J, Cole GM, et al. Inflammation and Alzheimer's disease. Neurobiol Aging. 2000;21:383–421.
44. Thurgur H, Pinteaux E. Microglia in the Neurovascular Unit: Blood-Brain Barrier-microglia Interactions After Central Nervous System Disorders. Neuroscience. 2019;405:55–67.

45. Li H, Liu CC, Zheng H, Huang TY. Amyloid, tau, pathogen infection and antimicrobial protection in Alzheimer's disease-conformist, nonconformist, and realistic prospects for AD pathogenesis. Transl Neurodegener. 2018;7:34.
46. Lee EB, Skovronsky DM, Abtahian F, Doms RW, Lee VMY. Secretion and intracellular generation of truncated Abeta in beta-site amyloid-beta precursor protein-cleaving enzyme expressing human neurons. J Biol Chem. 2003;278:4458–66.
47. De Strooper B. Lessons from a failed γ-secretase Alzheimer trial. Cell. 2014;159:721–6.
48. Piyoosh S, Pavan S, Anki S, Tripathi PN, Banerjee AG, Shrivastava SK. Comprehensive review of mechanisms of pathogenesis involved in Alzheimer's disease and potential therapeutic strategies. Prog Neurobiol. 2019;174:53–89.
49. Chen GF, Xu TH, Yan Y, Zhou YR, Jiang Y, Melcher K, et al. Amyloid beta: structure, biology and structure-based therapeutic development. Acta Pharmacol Sin. 2017;38:1205–35.
50. Alavi Naini SM, Soussi-Yanicostas N. Tau Hyperphosphorylation and Oxidative Stress, a Critical Vicious Circle in Neurodegenerative Tauopathies? Oxid Med Cell Longev. 2015;2015:151979.
51. Zhou H, Gong Y, Liu Y, Huang A, Zhu X, Liu J, et al. Intelligently thermoresponsive flower-like hollow nano-ruthenium system for sustained release of nerve growth factor to inhibit hyperphosphorylation of tau and neuronal damage for the treatment of Alzheimer's disease. Biomaterials. 2020;237:119822.
52. Zhou XW, Li X. Bjorkdahl C. Assessments of the accumulation severities of amyloid β-protein and hyperphosphorylated tau in the medial temporal cortex of control and Alzheimer's brains. Neurobiol Dis. 2006;22:657–68.
53. Louneva N, Cohen JW, Han LY, Tallbot K, Wilson RS, Bennett DA, et al. Caspase-3 is enriched in postsynaptic densities and increased in Alzheimer's disease. Am J Pathol. 2008;173:1488–95.
54. Braithwaite SP, Schmid RS, He DN, Sung A, Cho ML, Resnick S. L, et al. Inhibition of c-Jun kinase provides neuroprotection in a model of Alzheimer's disease. Neurobiol Dis. 2010;39:311–7.
55. Zhou Q, Wang M, Du Y, Zhang W, Bai M, Zhang Z, et al. Inhibition of c-Jun N-terminal kinase activation reverses Alzheimer disease phenotypes in APPswe/PS1dE 9 mice. Ann Neurol. 2015;77:637–54.
56. Thakur A, Wang XL, Siedlak SL, Perry G, Smith MA, Zhu XW. c-Jun phosphorylation in Alzheimer disease. J Neurosci Res. 2007;85:1668–73.
57. Ploia A, Antoniou X, Sclip A. JNK plays a key role in tau hyperphosphorylation in Alzheimer's disease models. J Alzheimers Dis. 2011;26:315–29.
58. Chu J, Lauretti E, Pratico D. Caspase-3-dependent cleavage of Akt modulates tau phosphorylation via GSK3beta kinase: Implications for Alzheimer's disease. Mol Psychiatry. 2017;22:1002–8.
59. Phiel CJ, Wilson CA, Lee VM, Klein PS. GSK-3α regulates production of Alzheimer's disease amyloid-β peptides. Nature. 2003;423:435.

60. Pei JJ, Braak H, Grundke-Iqbal I, Iqbal K, Winblad B, Cowburn RF. Distribution of active glycogen synthase kinase 3beta (GSK-3β) in brains staged of Alzheimer disease neurofibrillary changes. J Neuropathol Exp Neurol. 1999;58:1010–9.
61. Jeon S, Park JE, Lee J, Liu QF, Jeong HJ, Pak SC, et al. Illite improves memory impairment and reduces Ab level in the Tg-APPswe/PS1dE9 mouse model of Alzheimer's disease through Akt/CREB and GSK-3b phosphorylation in the brain. J Ethnopharmacol. 2015;160:69–77.
62. Hanger DP, Noble W. Functional implications of glycogen synthase kinase-3-mediated tau phosphorylation. Int J Alzheimers Dis. 2011;2011:352805.
63. Feng Y, Xia Y, Yu G, Shu X, Ge H, Zeng K, et al. Cleavage of GSK-3beta by calpain counteracts the inhibitory effect of Ser9 phosphorylation on GSK-3β activity induced by H_2O_2. J Neurochem. 2013;126:234–42.
64. Bertrand J, Thieffine S, Vulpetti A, Cristiani C, Valsasina B, Knapp S, et al. Structural characterization of the GSK-3β active site using selective and non-selective ATP-mimetic inhibitors. J Mol Biol. 2013;333:393–407.
65. Lai KO, Ip NY. Cdk5: a key player at neuronal synapse with diverse functions. Mini Rev Med Chem. 2015;15:390–5.
66. Tsai LH, Delalle I, Caviness VS Jr, Chae T, Harlow E. p35 is a neural-soecific regulatory subunit of cyclin-dependent kinase 5. Nature. 1994;371:419–23.
67. Sadleir KR, Vassar R. Cdk5 protein inhibition and Ab42 increase BACE1 protein level in primary neurons by a post-transcriptional mechanism: implications of CDK5 as a therapeutic target for Alzheimer disease. J Biol Chem. 2012;287:7224–35.
68. Tsai LH, Lee MS, Cruz J. Cdk5, a therapeutic target for Alzheimer's disease? Biochim Biophy Acta. 2004;1697:137–42.
69. Kimura T, Ishiguro K, Hisanaga S. Physiological and pathological phosphorylation of tau by Cdk5. Front Mol Neurosci. 2014;7:65.
70. Iijima K, Ando K, Takeda S, Satoh Y, Seki T, Itohara S, et al. Neuron-specific phosphorylation of Alzheimer's beta-amyloid precursor protein by cyclin-dependent kinase 5. J Neurochem. 2000;75:1085–91.
71. Ishiguro K, Sato K, Takamatsu M, Park J, Uchida T, Imahori K. Analysis of phosphorylation of tau with antibodies specific for phosphorylation sites. Neurosci Lett. 1995;202:81–4.
72. Fu PF, Gao M, Yung KKL. Association of intestinal disorders with Parkinson's disease and Alzheimer's disease: a systematic review and meta-analysis. ACS Chem Neurosci. 2020;11:395–405.
73. Bostanciklioğlu M. The role of gut microbiota in pathogenesis of Alzheimer's disease. J Appl Microbiol. 2019;127:954–67.
74. Vogt NM, Kerby RL, Dill-McFarland KA, Harding SJ, Merluzzi AP, Johnson SC, et al. Gut microbiome alterations in Alzheimer's disease. Sci Rep. 2017;7:13537.

75. Haran JP, Bhattarai SK, Foley SE, Dutta P, Ward DV, Bucci V, et al. Alzheimer's disease microbiome is associated with dysregulation of the anti-inflammatory P-glycoprotein pathway. mBio. 2019;10:e00632-19.
76. Cattaneo A, Cattane N, Galluzzi S, Provasi S, Lopizzo N, Festari C, et al. Association of brain amyloidosis with pro-inflammatory gut bacterial taxa and peripheral inflammation markers in cognitively impaired elderly. Neurobiol Aging. 2016;49:60–8.
77. Harach T, Marungruang N, Duthilleul N, Cheatham V, Mc Coy KD, Frisoni G, et al. Reduction of Abeta amyloid pathology in APPPS1 transgenic mice in the absence of gut microbiota. Sci Rep. 2017;7:41802.
78. Takiishi T, Fenero CIM, Camara NOS. Intestinal barrier and gut microbiota: Shaping our immune responses throughout life. Tissue Barriers. 2017;5:e1373208.
79. Sadia K, Thomson PJ, Lawrence O, Ren XM, Li MQ, Xin Y. A poly-saccharide isolated from dictyophora indusiata promotes recovery from antibiotic-driven intestinal dysbiosis and improves gut epithelial barrier function in a mouse model. Nutrients. 2018;10:1003.
80. Laparra JM, Sanz Y. Bifidobacteria inhibit the inflammatory response induced by gliadins in intestinal epithelial cells via modifications of toxic peptide generation during digestion. J Cell Biochem. 2010;109:801–7.
81. Matsuoka K, Kanai T. The gut microbiota and inflammatory bowel disease. Semin Immunopathol. 2015;37:47–55.
82. Zhang LL, Chen X, Zheng PY, Luo Y, Lu GF, Liu ZQ, et al. Oral Bifidobacterium modulates intestinal immune inflammation in mice with food allergy. J Gastroenterol Hepatol. 2010;25:928–34.
83. Orbe-Orihuela YC, Lagunas-Martínez A, Bahena-Román M, Madrid-Marina V, Torres-Poveda K, Flores-Alfaro E, et al. High relative abundance of firmicutes and increased TNF-α levels correlate with obesity in children. Salud Publica Mex. 2017;60:5–11.
84. Kobayashi Y, Sugahara H, Shimada K, Mitsuyama E, Kuhara T, Yasuoka A, et al. Therapeutic potential of Bifidobacterium breve strain A1 for preventing cognitive impairment in Alzheimer's disease. Sci Rep. 2017;7:13510.
85. Bäuerl C, Collado MC, Diaz Cuevas A, Viña J, Pérez Martínez G. Shifts in gut microbiota composition in an APP/PSS1 transgenic mouse model of Alzheimer's disease during lifespan. Lett Appl Microbiol. 2018;66:464–71.
86. Wang M, Amakye WK, Guo L, Gong C, Zhao Y, Yao M, et al. Walnut-derived peptide PW5 ameliorates cognitive impairments and alters gut microbiota in APP/PS1 transgenic mice. Mol Nutr Food Res. 2019;63:e1900326.
87. Roubaud-Baudron C, Krolak-Salmon P, Quadrio I, Mégraud F, Salles N. Impact of chronic Helicobacter pylori infection on Alzheimer's disease: preliminary results, Neurobiol. Aging. 2012;33:e11–9.
88. Wang XL, Zeng J, Yang Y, Xiong Y, Zhang ZH, Qiu M, et al. Helicobacter pylori filtrate induces Alzheimer-like tau hyperphosphorylation by activating glycogen synthase kinase-3β. J Alzheimers Dis. 2015;43:153–65.

89. Ijssennagger N, Belzer C, Hooiveld GJ, Dekker J, van Mil SW, Müller M, et al. Gut microbiota facilitates dietary heme-induced epithelial hyperproliferation by opening the mucus barrier in colon. Proc Natl Acad Sci USA. 2015;112:10038–43.
90. Derrien M, Belzer C, De Vos WM. Akkermansia muciniphila and its role in regulating host functions. Microb Pathog. 2017;106:171–81.
91. Hidalgo-Cantabrana C, Delgado S, Ruiz L, Ruas-Madiedo P, Sanchez B, Margolles A. Bifidobacteria and their health-promoting effects. Microbiol Spectr. 2017. doi:10.1128/microbiolspec.

Figures

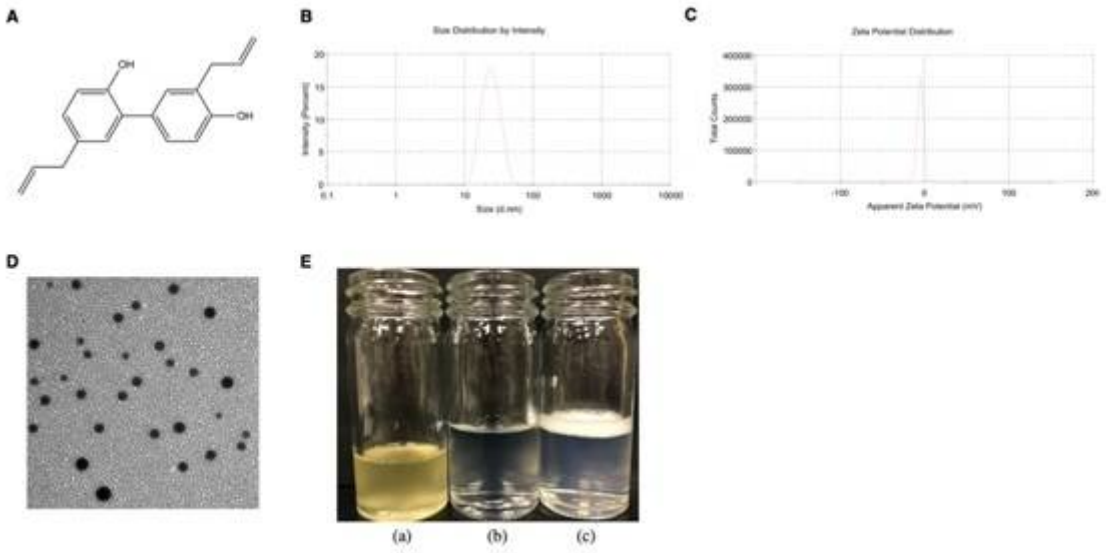

Figure 1

(A) Chemical structure of HO. (B) Particle size and distribution of Nano-HO(n = 3). (C) Zeta potential of Nano-HO(n = 3). (D) TEM image of Nano-HOdroplet. (E) Appearance of the Nano-HOasstocking solution (a), as working solution that diluted 100-fold with distilled water (b) and HO solution thatsuspended in 0.5% CMC-Na (c).

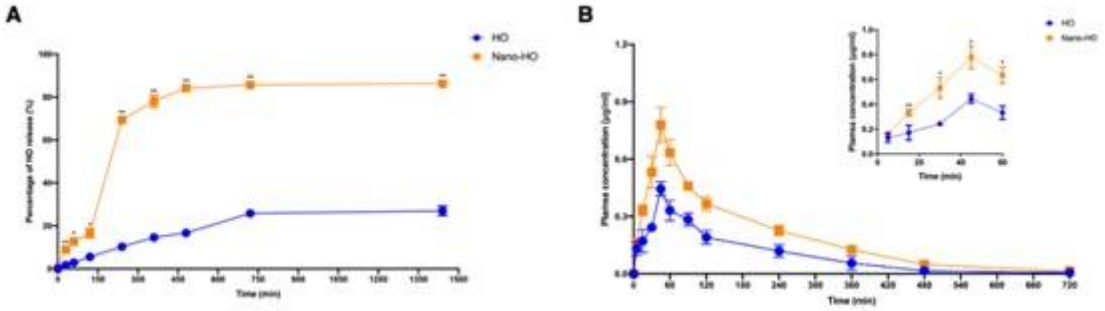

C

Parameters	HO	Nano-HO
AUC_{0-12} (μg·h/mL)	1.18 ± 0.05	2.20 ± 0.06 **
$t_{1/2}$ (h)	1.09 ± 0.22	1.63 ± 0.31
T_{max} (h)	0.80 ± 0.07	0.78 ± 0.05
C_{max} (ng/mL)	0.44 ± 0.02	0.78 ± 0.09 **
MRT_{0-12} (h)	2.58 ± 0.10	2.83 ± 0.15
Relative bioavailability (%)	-	186.44%

Figure 2

In vitro release and pharmacokinetic profiles of Nano-HO and HO. (A) In vitro release of Nano-HO and HO in PBS (pH 7.4); (B) Plasma concentration-time profiles of rats after oral administration with Nano-HO (80 mg/kg) and HO (80 mg/kg);(C) Pharmacokinetics parameters after oral administration with Nano-HO (80 mg/kg) and HO (80 mg/kg).Data are expressed as mean ± SEM(n = 5). *p<0.05 and **p<0.01 ascompared withregular HOgroup.

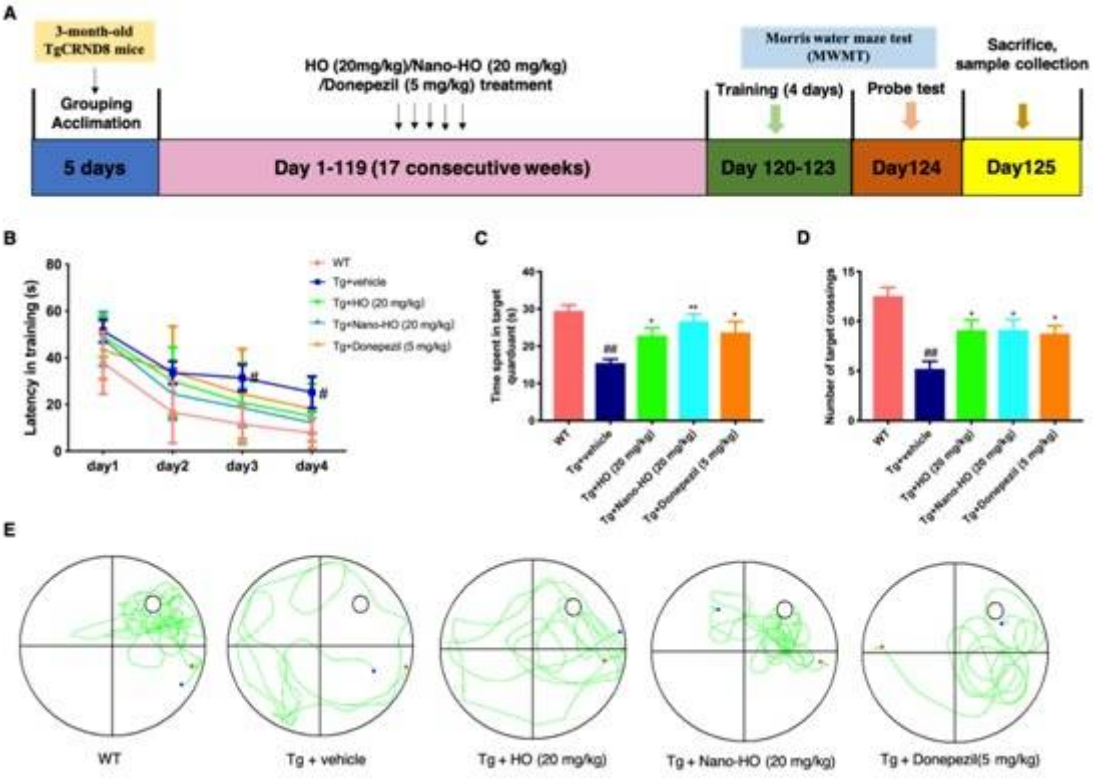

Figure 3

Effects of Nano-HO and HO on the spatial learning and memory functions of TgCRND8 mice. The spatial learning and memory functions were evaluated using MWMT. (A) Experimental design and treatment schedule to evaluate the neuroprotective effects of HO and Nano-HO on TgCRND8 transgenic mice; (B) The latency to find a hidden platform during 4 consecutive days of training; (C) Time spent in the target quadrant; (D) Number of target crossings; (E) Representative swimming tracks of mice in the probe test. Data were expressed as mean ± SEM (n = 9). #p< 0.05 and ##p< 0.01 when compared with the WT group; * p< 0.05 and ** p< 0.01 when compared with the Tg + vehicle group.

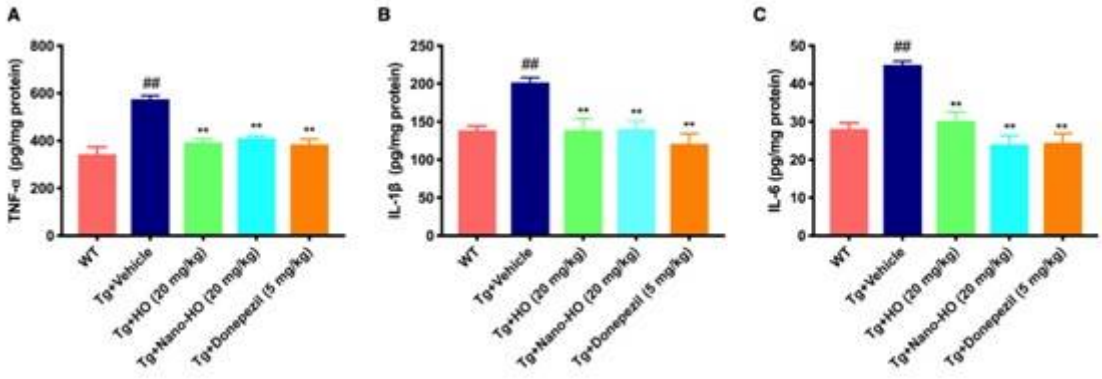

Figure 4

Effects of Nano-HO and HO on the levels of cytokines includingTNF-α (A), IL-1β (B) and IL-6 (C) in the brain tissues of TgCRND8 mice. Data were expressed as mean ± SEM (n = 6). ##p< 0.01 compared with WT group; ** p< 0.01 compared with Tg + vehicle group.

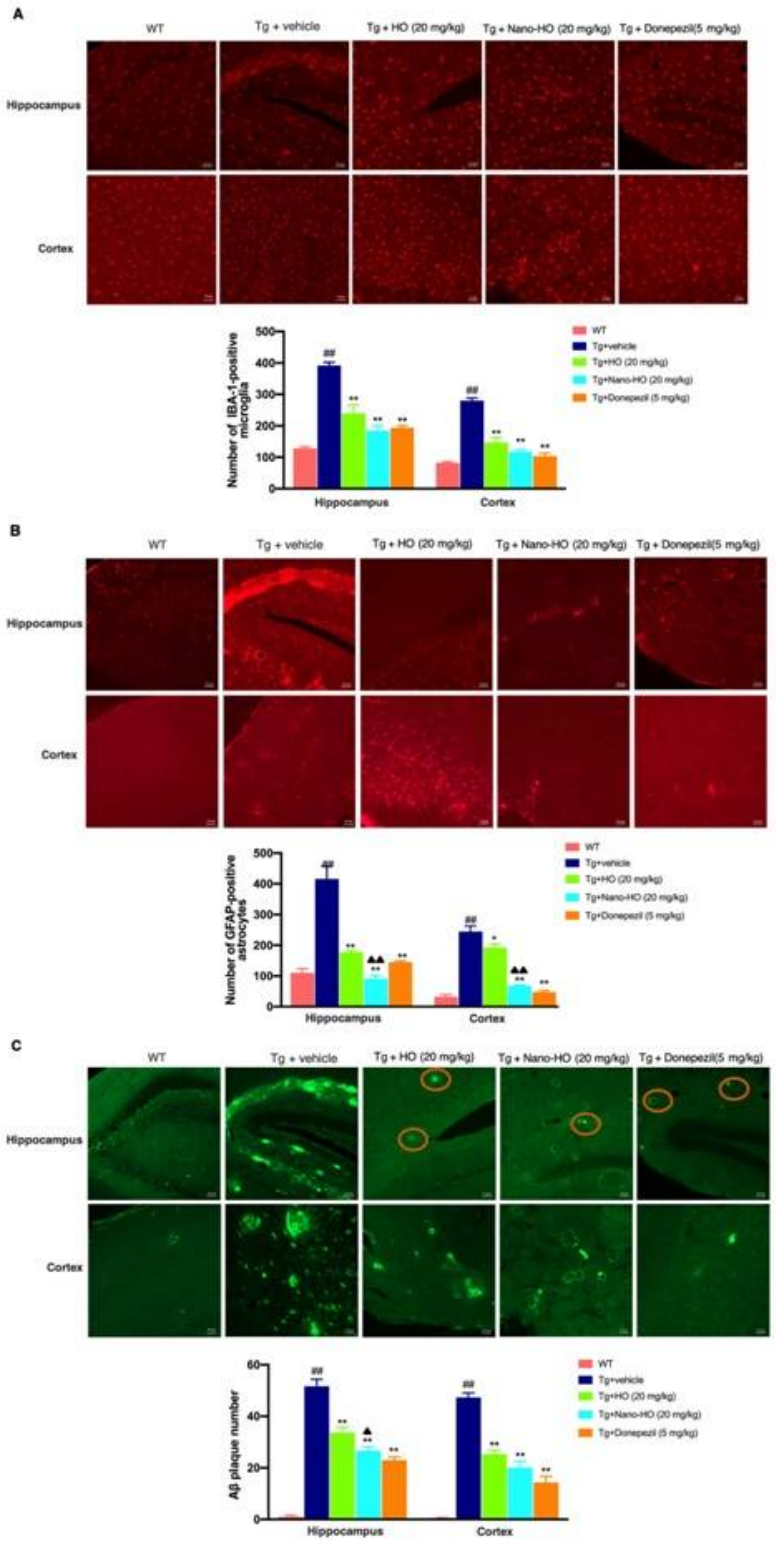

Figure 5

Effects of Nano-HO and HO on IBA-1 positive microglia (A), GFAP-positive astrocytes (B) and Aβ deposits (C) in the hippocampus and cortex of TgCRND8 mice. The number of IBA-1-positive microglia, GFAP-positive astrocytes and the Aβ plaques were measured respectively. Magnification: 200*. Data were expressed as mean ± SEM (n = 3). ##p< 0.01 when compared with the WT group; * p< 0.05 and ** p< 0.01

when compared with the Tg + vehicle group; ▲p< 0.01 and ▲▲p< 0.01 when compared with Nano-HO group.

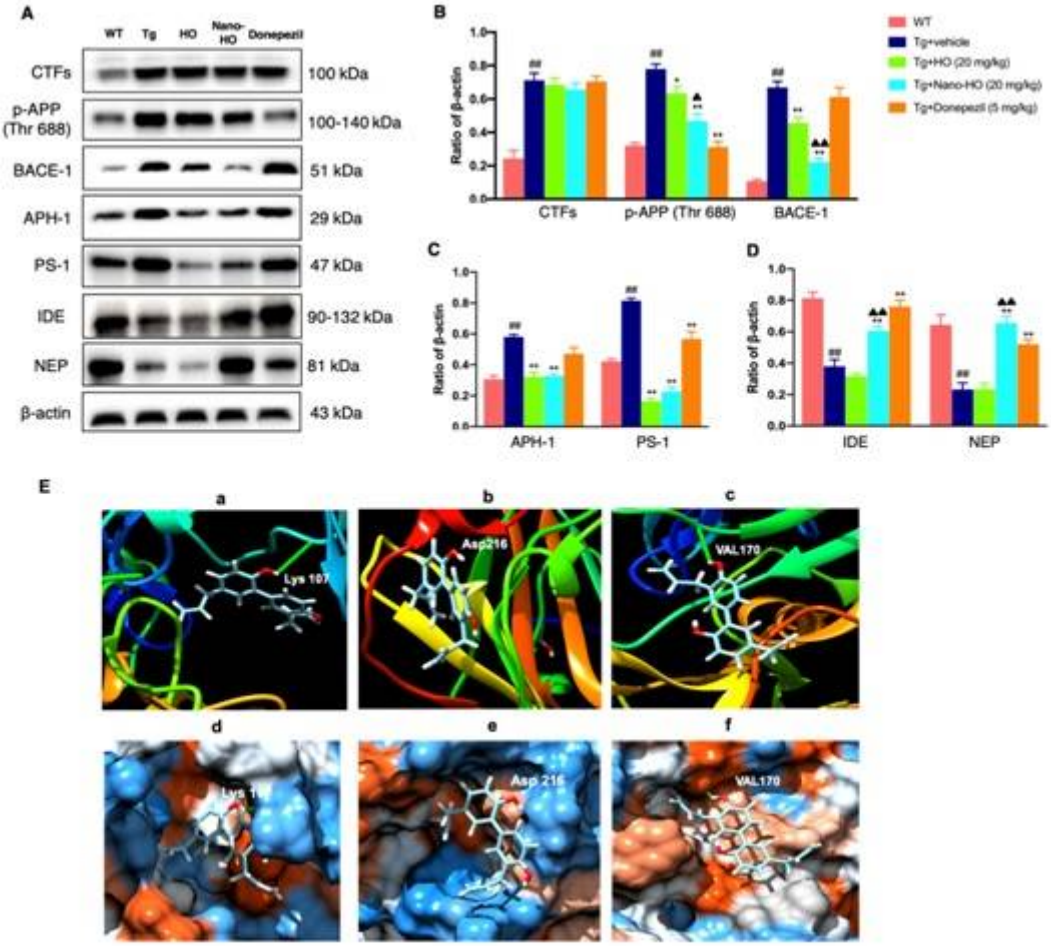

Figure 6

Effects of Nano-HO and HO on the APP processing and APP phosphorylation in the brain tissues of TgCRND8 mice. (A) Representative western blotting images of the protein expressions of CTFs, p-APP (Thr 688), BACE-1, APH-1, PS-1, IDE and NEP. (B) Quantitative analysisof the protein expressions of CTFs, p-APP (Thr 688) and BACE-1. (C) Quantitative analysisof the protein expressions of APH-1 and PS-1. (D) Quantitative analysisof the protein expressions of IDE and NEP. (E) Molecular docking analysis of HO with BACE-1 protein. (a-c) The surface-docking model of honokiol in the BACE-1 active sites (Lys 107, Asp 216 and VAL 170, respectively); (d-f) Ribbon representation (3D) of the BACE-1 protein structures along with binding of HO (Lys 107, Asp 216 and VAL 170, respectively). Data were expressed as mean ± SEM (n = 3). ##p< 0.01 when compared with the WT group; * p< 0.05 and ** p < 0.01 when compared with the Tg + vehicle group; ▲ p< 0.05 and ▲▲p< 0.01 when compared with HO group.

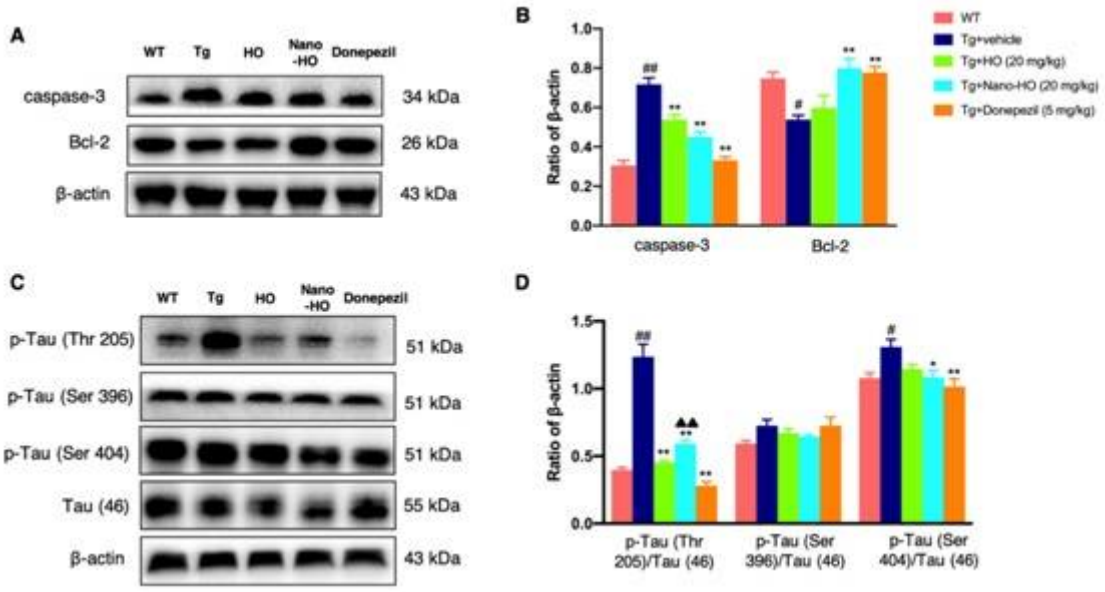

Figure 7

Effects of Nano-HO and HO on apoptosis andtau protein hyperphosphorylation in the brain tissues of TgCRND8 mice. (A) Representative western blotting images of the caspase-3 and Bcl-2 protein expressions. (B) Quantitative analysis the protein expressions of the caspase-3 and Bcl-2. (C) Representative western blotting images of the p-Tau (Thr 205), p-Tau (Ser 396), p-Tau (Ser 404) and tau (Tau 46) protein expressions. (D) Quantitative analysis the ratios of p-Tau (Thr 205)/tau (46), p-Tau (Ser 396)/tau (46) and p-Tau (Ser 404)/tau (46). Data were expressed as mean ± SEM (n = 3). #p< 0.05 and ## p< 0.01 when compared with the WT group; * p< 0.05 and ** p< 0.01 when compared with the Tg + vehicle group; ▲▲p< 0.01 when compared with HO group.

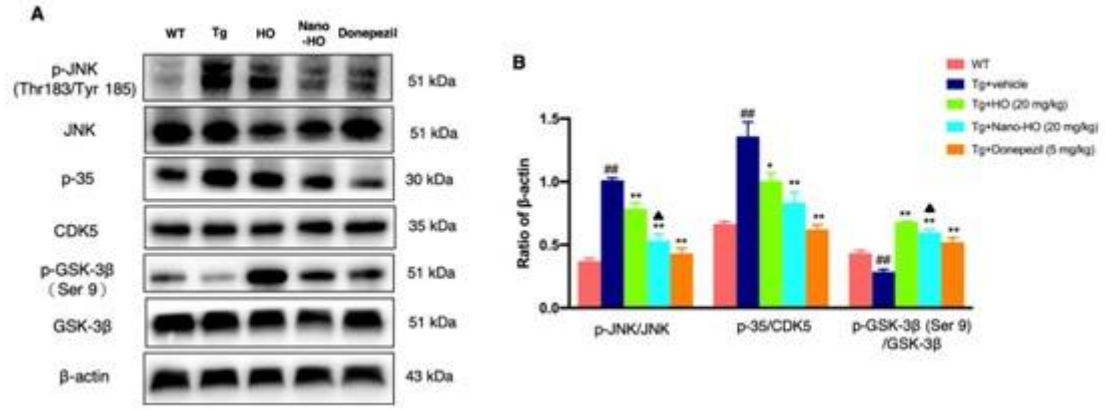

Figure 8

Effects of Nano-HO and HO on JNK/CDK5/GSK-3β signaling pathway in the brain tissues of TgCRND8 mice. (A) Representative western blotting images of the protein expressions of p-JNK, JNK, p-35, CDK5, p-GSK-3β (Ser 9) and GSK-3β. (B) Quantitative analysisof the radios of p-JNK/JNK, p-35/CDK5 and p-GSK-3β (Ser 9)/GSK-3β. Data were expressed as mean ± SEM (n = 3). ## p< 0.01 when compared with the WT

group; * p< 0.05 and ** p< 0.01 when compared with the Tg + vehicle group; ▲ p< 0.05 when compared with HO group.

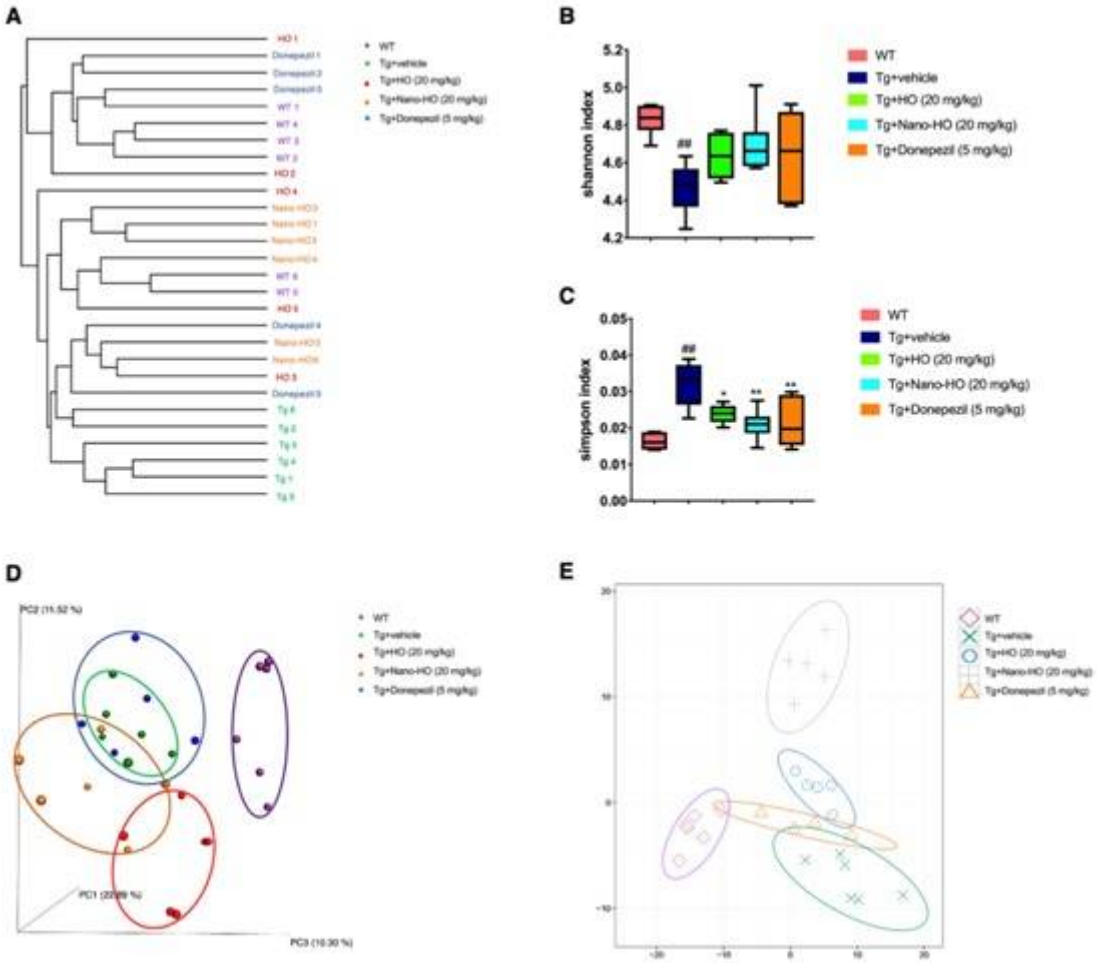

Figure 9

Differences in gut microbiota profiles among the five groups. (A) The system clustering tree. (B) The Shannon index. (C) The Simpson index. (D) PCoA analysis of gut bacteria (PC1 versus PC2). (E) PLS-DA analysis of gut bacteria. Data were expressed as mean ± SEM (n = 5-6). ## p< 0.01 when compared with the WT group; * p< 0.05 and ** p< 0.01 when compared with the Tg + vehicle group.

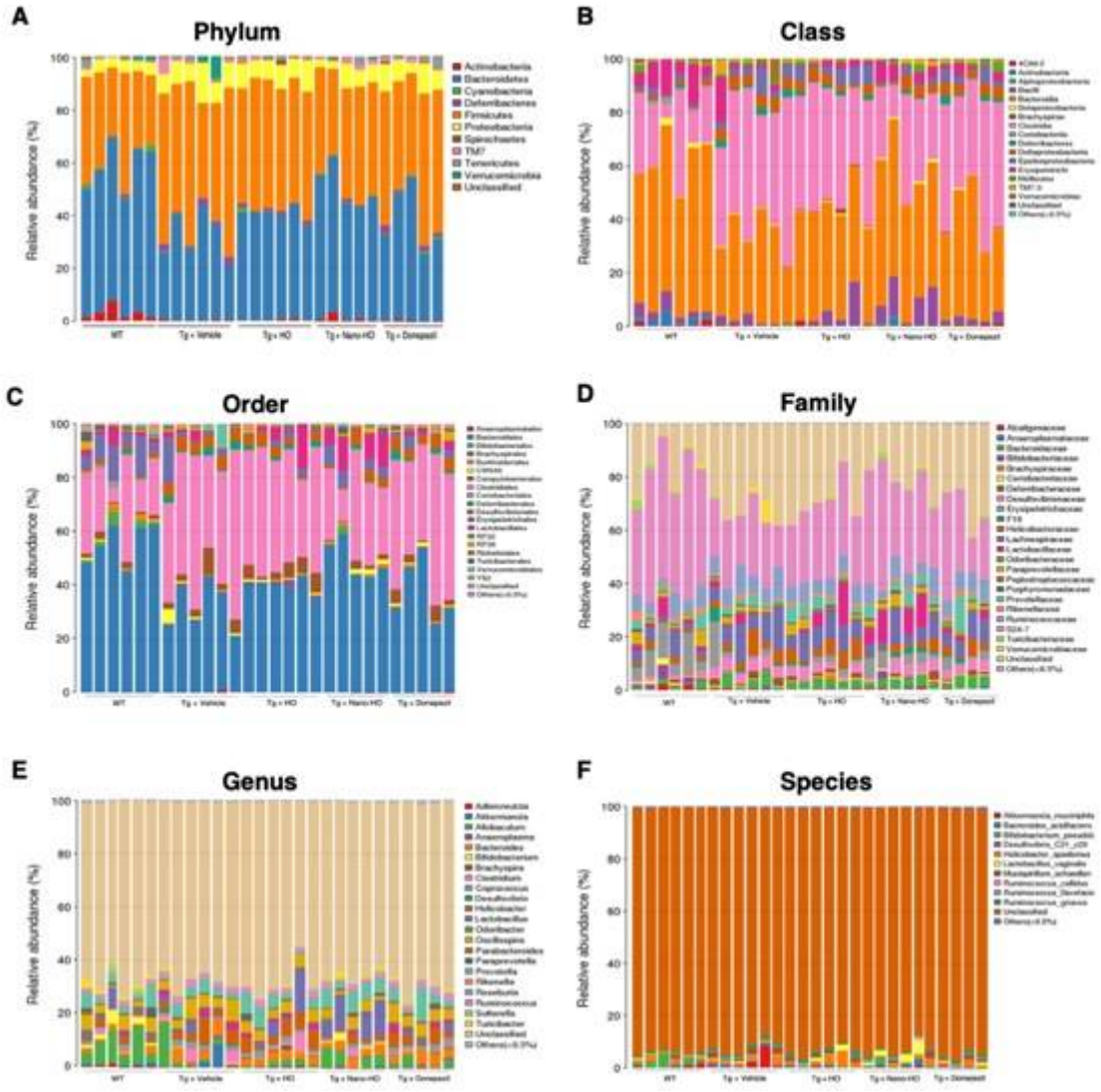

Figure 10

The taxonomic composition of fecal bacterial community structure in mice. The relative abundance of fecal microbiota of the taxonomic levels (A) phylum, (B) class, (C) order, (D) family, (E) genus, and (F) species (n = 6).

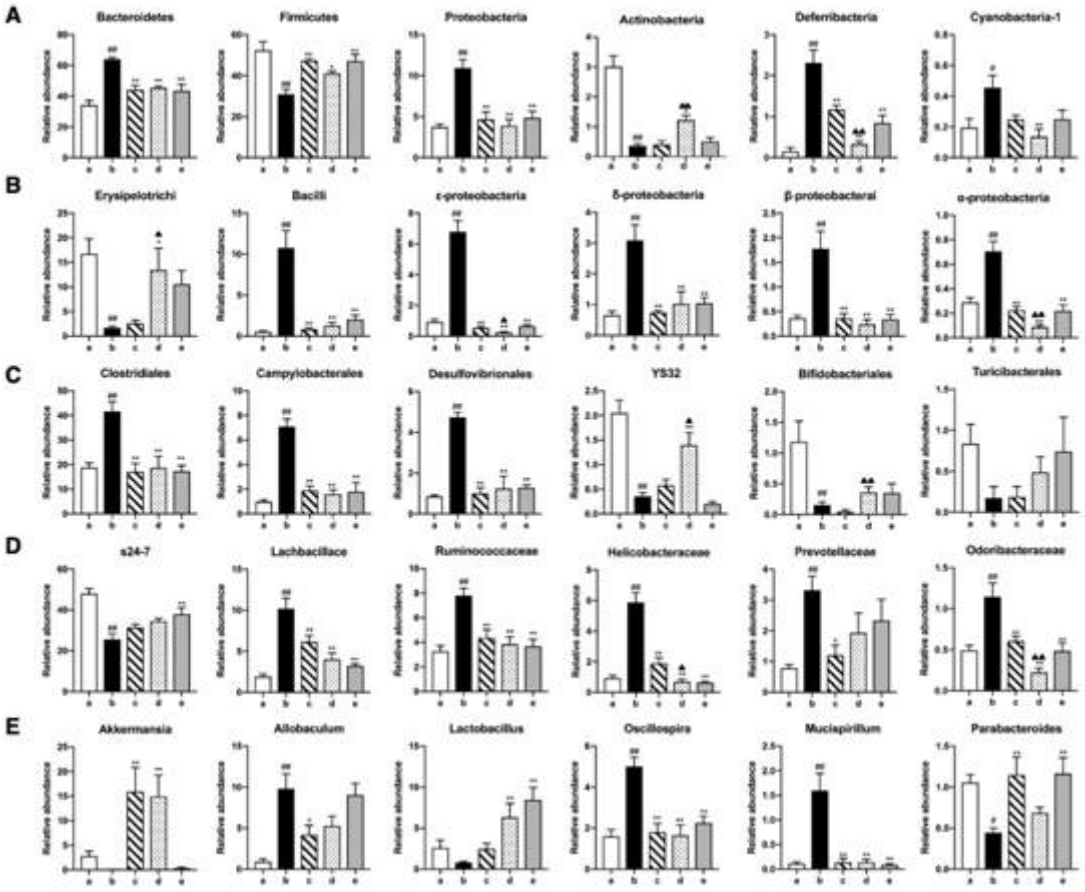

Figure 11

Differences in the relative abundance of various gut microbes among WT, Tg and HO treatment groups. Relative abundances of (A) phylum, (B) class, (C) order, (D) family, and (E) genus. (a. WT group; b. Tg + vehicle group; c. Tg +HOgroup; d. Tg + Nano-HO group; e. Tg + Donepezil group). Data were shown as mean ± SEM (n = 6). # p< 0.05 and ## p< 0.01 when compared with the WT group; * p< 0.05 and ** p< 0.01 when compared with the Tg + vehicle group; ▲ p< 0.05 and ▲▲ p< 0.01 when compared with the HO group.

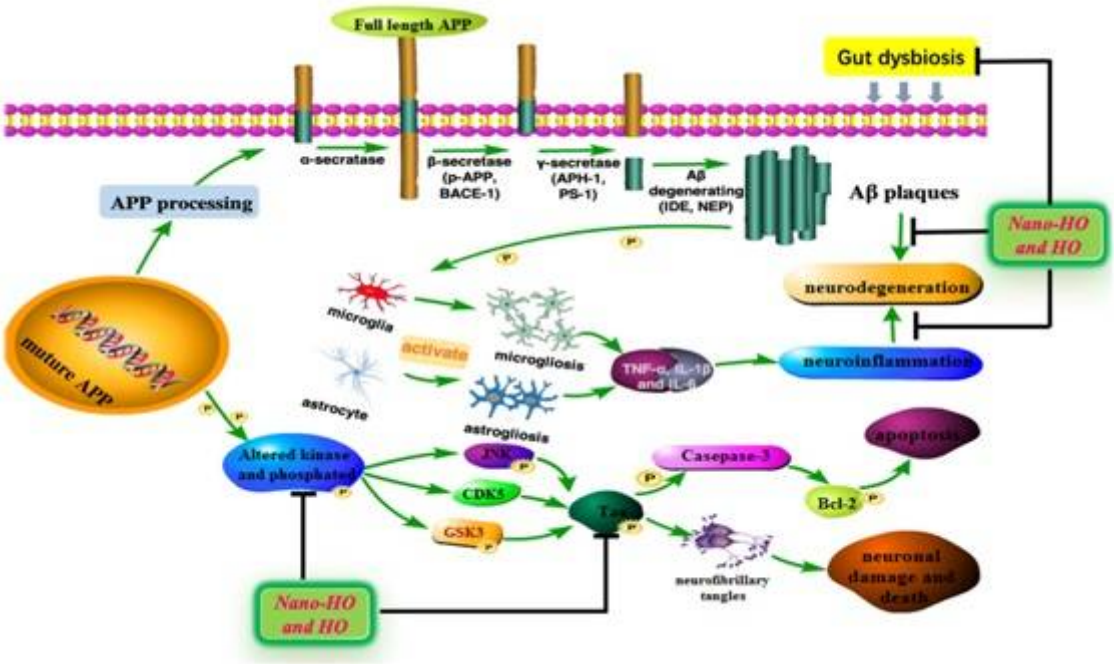

Figure 12

A schematic drawing depicting the molecular mechanisms underlying the cognitive deficits ameliorating actions of Nano-HO and HO in TgCRND8 mice. Firstly, the transmembrane APP was processed in the amyloidogenic pathway, in which APP was sequentially cleaved by β-secretase, γ-secretase and Aβ degrading enzymes, leading to the production of Aβ peptide and formation of Aβ plaques. Nano-HO and HO reduced Aβ deposition by inhibiting β-secretase andγ-secretase and enhancing theactivity of Aβ degrading enzymes, thereby reducing the Aβ-associated activation of microgliosis and astrogliosis, as well as decreasing secretion of pro-inflammatory cytokines. Also, Nano-HO and HO inhibit tau hyperphosphorylationvia preventing the activation of JNK/CDK5/GSK-3β signaling pathway and preventing apoptosis. Moreover, Nano-HO and HO regulated the gut dysbiosis to reach a balance and protect the microbiota flora stability in TgCRND8 mice. These molecular actions of Nano-HO and HO finally contributed to the improvements in spatial learning and memory therapeutic effects in TgCRND8 mice.

Supplementary Files

This is a list of supplementary files associated with this preprint. Click to download.

- GraphicalAbstract.jpg